Constraining Dark Matter with Gravitational Waves from Supermassive Black Hole Binaries using Cassini Data

Bachelorarbeit

zur Erlangung des akademischen Grades
Bachelor of Science in Physik
am Institut für Theoretische Physik
der Goethe-Universität in Frankfurt am Main

vorgelegt von
Matthias Daniel

eingereicht am 10. August 2023

https://doi.org/10.21248/gups.79949

Selbstständigkeitserklärung

Hiermit erkläre ich, dass ich die Arbeit selbstständig und ohne Benutzung anderer als der angegebenen Quellen und Hilfsmittel verfasst habe. Alle Stellen der Arbeit, die wörtlich oder sinngemäß aus Veröffentlichungen oder aus anderen fremden Texten entnommen wurden, sind von mir als solche kenntlich gemacht worden. Ferner erkläre ich, dass die Arbeit nicht - auch nicht auszugsweise - für eine andere Prüfung verwendet wurde.

Erlenbach am Main, den 10. August 2023

_____

Matthias Daniel

Contents

1 Introduction

1.1 Gravitational Waves and Dark Matter

"Ladies and gentlemen, we have detected gravitational waves! We did it!"

- David Reitze, executive director of the LIGO Laboratory [1]

On September 14, 2015, marking a century since the final establishment of general relativity (GR) by Albert Einstein, the time had finally come: The first confirmed gravitational wave signal was directly detected concurrently by the two detectors of the Laser Interferometer Gravitational-Wave Observatory (LIGO) located in Hanford, Washington and Livingston, Louisiana. These gravitational waves were emitted during the coalescence of two black holes with stellar masses of $35\,M_\odot$ and $30\,M_\odot$, respectively, resulting in the formation of a single black hole with a mass of $62\,M_\odot$ at a luminosity distance of 440 Mpc [2]–[4].

Gravitational waves (GWs) are tiny distortions of four-dimensional spacetime that propagate as waves at the speed of light c and are solutions to the linear approximation of Einstein's field equations (see Chapter 2.4). Strong sources of GWs include binary systems of compact objects such as neutron stars, black holes, or a mixture of both. Additionally, supernovae and potentially cosmological first-order phase transitions in the early universe can also produce GWs [5]. Similar to electromagnetic waves, GWs can be characterized by their frequency, polarization, direction, and amplitude. The frequency of a GW varies depending on the properties of its source, resulting in different frequency ranges. To capture the entire GW spectrum depicted in Figure 1.1, not only ground-based detectors but also upcoming space-based detectors such as the Laser Interferometer Space Antenna (LISA) are utilized[1]. The amplitude of GWs, and consequently the characteristic strain (see Chapter 2.4), carries essential information, for instance, about the environment of the constituents of a binary system. By studying its GW signal, one can infer, for example, the possible existence of dark matter (DM) halos around the compact objects, which could significantly influence the orbital evolution of the system, primarily through the dynamical friction mechanism (see Chapter 2.3.2). As a result, the components of the binary system gradually approach each other and the intensity and phase of the GWs are altered compared to the idealized case where the objects are surrounded by vacuum.

[1] The current detectors of GWs usually work on the principle of a Michelson interferometer.

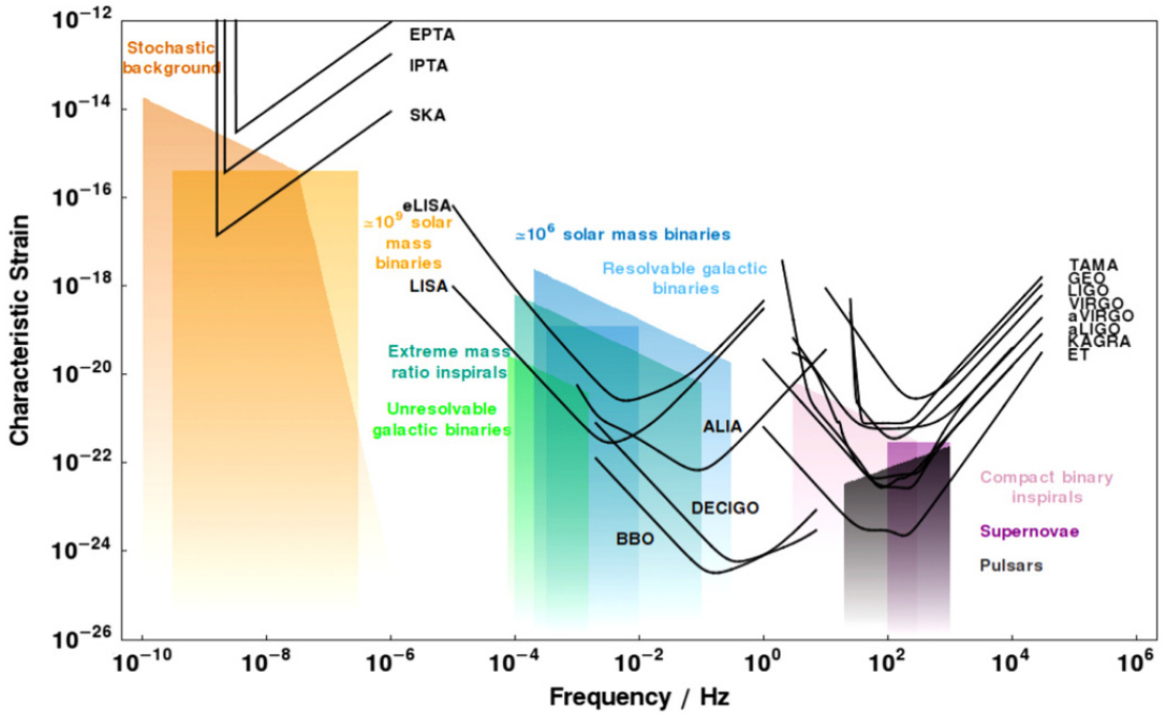

Fig. 1.1: Gravitational wave spectrum. Plot of the sensitivity curves[2] for different detectors and of the characteristic strain against frequency for a variety of astrophysical and cosmological sources [6].

The fundamental characteristics and selected indications for the existence of DM are outlined below. DM is a theoretical form of matter that does not interact with photons through absorption, reflection, or emission, and therefore appears *dark* or invisible to conventional telescopes. The specific nature of DM particles remains unknown at present.

Observations of galaxy rotation curves [7] or gravitational lensing [8] by a large accumulation of matter can be accounted for only through the existence of additional, unseen matter; the presence of visible matter alone is inadequate to explain these phenomena. Furthermore, DM is invoked in explaining the current large-scale structures of the universe and the closely associated formation and evolution of galaxy clusters [9].

Despite numerous theories regarding the properties of DM (cf. Figure 2.1), there is still no direct evidence for its existence. In Chapter 2.1 the most important DM models for this bachelor thesis are presented. These include cold dark matter (CDM) and self-interacting dark matter (SIDM).

[2]Sensitivity curve: It shows how sensitive a detector is to a GW signal at a certain frequency. The signal can be detected by the corresponding detector, only for the frequency range in which the GW spectrum of a source is above this curve.

Some astrophysicists, on the other hand, propose an alternative hypothesis that DM does not consist of particles beyond the Standard Model of particle physics. Instead, they assume that the gravitational theory formulated by Einstein or Newton is incomplete, and therefore, they attempt to generalize it. In this so-called *modified gravity theory* or *modified Newtonian dynamics*, Einstein's field equations or Newton's law of gravitation are modified to explain successfully the aforementioned observations[3] (cf. [10], [11]) and other phenomena [12].
However, these modified theories cannot fully or convincingly explain all observations, such as those of the Bullet Cluster (1E 0657-558) [13]. Therefore, in this work it is assumed that DM is composed of particles.

1.2 Cassini Spacecraft and the Stochastic Gravitational Wave Background

As shown in Figure 1.1 there is currently no permanently available detector that can measure GWs in the micro- to millihertz frequency range. Here, the Cassini spacecraft comes into play. It is based on the Doppler tracking method for detecting or constraining the level of GWs. The detector operates on the principle that the Earth and a distant spacecraft act as separated test masses. A nearly monochromatic electromagnetic microwave signal is transmitted from the ground, phase-coherently transponded at the spacecraft, and subsequently received back on the ground. The Doppler tracking system determines the relative dimensionless velocity between the Earth and the spacecraft by comparing the frequencies of the transmitted and received signals. The Earth-spacecraft system is affected by the presence of GWs, resulting in Doppler perturbations. These disturbances ultimately allow the determination of the characteristic strain of the GW signal. From the respective data collected during the three 40-day-long Cassini missions in the years 2001/2002, 2002/2003, and 2003/2004, an upper limit for the isotropic stochastic gravitational wave background (GWB) in the frequency range of 10^{-6} to 10^{-3} Hz can be derived (see Chapter 4) [14], [15].
The GWB being referred to in this context is not the one that could potentially be a relic of specific cosmological events during the early stages of the universe's evolution (cf. Figure 1.1 and [5]), but rather the GWB generated by the incoherent superposition of GWs from a large number of widely spaced inspiraling supermassive black hole binaries (SMBHBs) in the late phase of their evolution. Due to the immense masses of their components, each ranging

[3]Specifically, the modified Newtonian dynamics (MOND) concept is remarkably effective in explaining the profiles of galactic rotation curves [9].

from 10^5 to $10^{10} M_\odot$, SMBHBs are among the most powerful known sources of GWs. While the frequency of GWs emitted by SMBHBs can initially be attributed to the nanohertz range, where the aforementioned cosmological GWB of primordial origin is also located, they enter the detectable frequency range of Cassini in the last years to days of their evolution, depending on their masses. These gravitational bound systems are formed through the merger of two galaxies, each harboring a supermassive black hole (SMBH) in its central region [2].

1.3 Motivation

For frequencies below about 10 Hz, it becomes difficult to protect ground-based detectors from seismic noise and the fluctuating gravitational forces caused by environmental factors [16]. Therefore, astrophysical information regarding SMBHBs and their environments remains inaccessible to any current Earth-based detector generation. Hence, the aim of this bachelor thesis is to examine the measurement data of the first 40-day observation by Cassini regarding the GWB in more detail to assess the likelihood of certain DM theories relative to others. In order to achieve this, a lower limit for the DM density around SMBHs is calculated using the upper limit on the characteristic strain of the GWB. This lower limit is then compared with the spike densities (cf. Chapter 2.2) in the case of CDM and SIDM. The Cassini data are particularly suitable for this purpose due to the rapid decrease in separation between the constituents of SMBHBs within the frequency range accessible to the spacecraft. This enables insights into an interesting stage of their evolution even within the relatively short observation period of Cassini.

In the subsequent sections, a concise summary will be provided for the two DM models mentioned earlier, along with an explanation of DM spikes around SMBHs (see Subsections 2.1 and 2.2). Following that, a mathematical and physical analysis will be conducted to describe the orbital evolution of SMBHBs and the GWs emitted during their progression (see Subsections 2.3 and 2.4). Before presenting and discussing the results of this work in Chapter 4, the Python code utilized for the numerical calculations will be introduced. In the last two chapters the findings of this study are summarized, and an outlook on future research in this field is provided.

2 Theoretical Background

2.1 Dark Matter Models

Figure 2.1 illustrates the diversity of DM theories, of which the two most relevant models for this work will be briefly presented. A detailed description of individual theories can be found, for example, in [9] or [17].

Fig. 2.1: Overview of some theories of DM from [18].

2.1.1 Cold Dark Matter

Cold dark matter (CDM) is the most common model, in which particles are assumed to move at non-relativistic speeds (*cold*) and interact weakly with any form of matter, making them collisionless. It is also part of the standard model of cosmology, known as the ΛCDM[4] model. Simulations using CDM have been successful in describing the large-scale structure formation and clustering of galaxies in the universe. However, they also encounter inconsistencies when it comes to observations regarding the distribution of DM in the inner regions of spiral galaxies (cf. [19]). This is known as the *core-cusp problem* [9].

[4]ΛCDM model: It describes the evolution of the universe as a flat spacetime structure, starting from the Big Bang up to the present day. Λ represents the cosmological constant, which could potentially be associated with dark energy.

J. Navarro, C. Frenk, and S. White (NFW), using N-body simulations with CDM, found that over time, spherically symmetric accumulations of DM, known as DM halos, can form around the centers of galaxies [20]. These NFW halos can be described using just two parameters, the scale radius r_s and the scale density ρ_s, according to

$$\rho_{NFW}(r) = \frac{\rho_s}{\frac{r}{r_s}\left(1+\frac{r}{r_s}\right)^2}, \tag{2.1}$$

where r represents the distance from the galactic center.
It can be seen that for small r, i.e., at the center of a galaxy, the density profile is proportional to r^{-1}, and consequently the density increases steadily for small r. This is referred to as a *cusp*. However, some observations of rotation curves suggest a constant density in the inner regions of galaxies, which is called a *core*.
One solution to this problem is the concept of self-interacting dark matter, which will be discussed in more detail in the next subsection. This offers the possibility of smoothing the density profile, as, for example, investigated in [21] and [22].

2.1.2 Self-Interacting Dark Matter

Self-interacting dark matter (SIDM) is an alternative theory of DM particles that exhibit strong interactions with each other. In [23], the authors propose that the core-cusp problem can be resolved by considering SIDM particles with a significant scattering cross-section (per DM particle mass) σ_m, while assuming negligible annihilation[5] or dissipation. The scattering leads to heat transfer between particles and thermalization[6] within the nucleus of a galaxy [9].
The results of such an analysis are shown in Figure 2.2. If σ_m exceeds the value of $10\,\mathrm{cm}^2\,\mathrm{g}^{-1}$, the halo can undergo a process called gravothermal collapse (see [25] for more details).
Moreover, the SIDM model is consistent with the predictions of CDM on large scales, as the density of DM, and hence the probability of self-interactions, decreases on these size scales [26].

[5]The high-energy electromagnetic signature from a potential self-annihilation process of DM particles can also be utilized as evidence for the existence of DM or to constrain its properties (see, for example, [24]).
[6]Thermalization occurs when physical bodies interact with each other in a sufficient stochastic manner, resulting in a thermal equilibrium state.

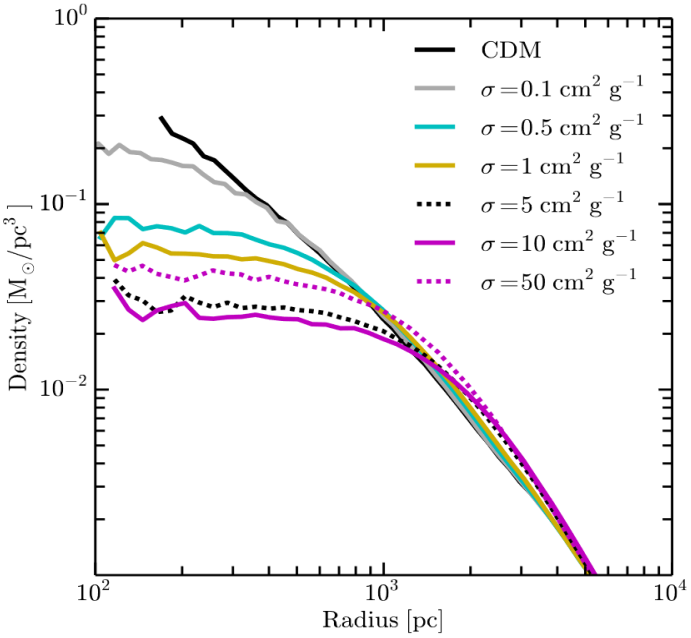

Fig. 2.2: SIDM particles with varying cross-sections (per DM particle mass) σ_m (here σ) can lead to the smoothing of the density profile in the inner regions of galaxies [27]. CDM produces a cusp.

2.2 Dark Matter Spikes around Supermassive Black Holes

Observations with ground-based telescopes as well as the Hubble Space Telescope reveal that most, if not all, galaxies host a SMBH in their central region [2]. In the following, it is assumed that the SMBHs are of the Schwarzschild type. If these SMBHs are embedded in DM halos, there is a possibility that the density distribution of the halos is strongly influenced by them. In particular, if a SMBH undergoes *adiabatic growth* over a timescale much longer than the orbital periods of the DM-halo particles, it is expected to result in a significant increase in the DM density around it. As a consequence, a so-called DM *spike* is formed [28]. This increase can be as large as 10 orders of magnitude within the region corresponding to the *sphere of influence* of the black hole (BH) [9], [29]. The spatial extent r_h (radius of the sphere of influence) of this region, where the gravitational attraction of the SMBH dominates over that of the host galaxy, is defined by

$$r_h = \frac{G\, m_{BH}}{\sigma^2}. \tag{2.2}$$

G denotes Newton's gravitational constant, m_{BH} the mass of the SMBH, and σ represents the velocity dispersion of the host galaxy-bulge.

Furthermore, this formula can be used to calculate the separation below which two SMBHs form a binary system. For this purpose, m_{BH} must be replaced by the total mass $M = m_{BH,1}+m_{BH,2}$ [30]. The DM spike density $\rho_{spike}(r)$ around a single SMBH can be described in the form of a power-law:

$$\rho_{spike}(r) = \begin{cases} 0 & , r < r_{min} \\ \rho_{sp}\left(\frac{r_{sp}}{r}\right)^{\alpha} & , r_h \geq r \geq r_{min} \end{cases}, \tag{2.3}$$

where ρ_{sp} is the normalization density, r_{sp} is the parameter of the spike size, which can be empirically defined by $r_{sp} \approx 0.2\, r_h$ [31], and α represents the slope of the profile. α is related to the slope $0 \leq \alpha_{ini} \leq 2$ of the initial cuspy halo density profile, i.e., the density profile before the adiabatic growth of the SMBH, according to the following equation [28]:

$$\alpha = \frac{9 - 2\alpha_{ini}}{4 - \alpha_{ini}}. \tag{2.4}$$

Based on this, the slope of the DM spikes takes the values $2.25 \leq \alpha \leq 2.5$. In the case of an initial CDM halo (NFW profile) with $\alpha_{ini} = 1$ (as explained in Subsection 2.1.1), the value for α_{CDM} is 7/3. Spikes formed from SIDM have a slope of $\alpha_{SIDM} = 7/4$ [32].
From the second definition of r_h,

$$M_{DM}(r < r_h) = 4\pi \int_0^{r_h} \rho_{spike}(r)\, r^2\, dr \overset{r_h \gg r_{min}}{\approx} 4\pi \int_0^{r_h} \rho_{sp} \left(\frac{r_{sp}}{r}\right)^{\alpha} r^2\, dr \overset{!}{=} 2\, m_{BH}, \tag{2.5}$$

an expression for ρ_{sp} can be derived [31]. It is given by

$$\rho_{sp} = \frac{(3-\alpha)\, 0.2^{3-\alpha}\, m_{BH}}{2\pi {r_{sp}}^3}. \tag{2.6}$$

Here it is assumed that the amount of baryonic matter compared to DM in the central region of a galaxy is negligibly small[7] and that $r_{sp} = 0.2\, r_h$ is valid (see above). In Equation (2.5) $M_{DM}(r < r_h)$ is the total mass of DM within the radius r_h around a SMBH.

[7] This assumption could be motivated by the fact that about 83.9 % of the **matter** in the universe is (C)DM according to [33].

Finally, in this work, r_{min} is equated with the innermost stable circular orbit (ISCO) of a Schwarzschild-BH, i.e.,

$$r_{min} = r_{ISCO} = 6\,\frac{G\,m_{BH}}{c^2}. \tag{2.7}$$

In Figure 2.3, the three different mentioned density profiles of DM are depicted. It can be seen that CDM produces the spike with the highest density. Furthermore, it is typical to model the CDM density for $r > r_h$ as the corresponding NFW profile.

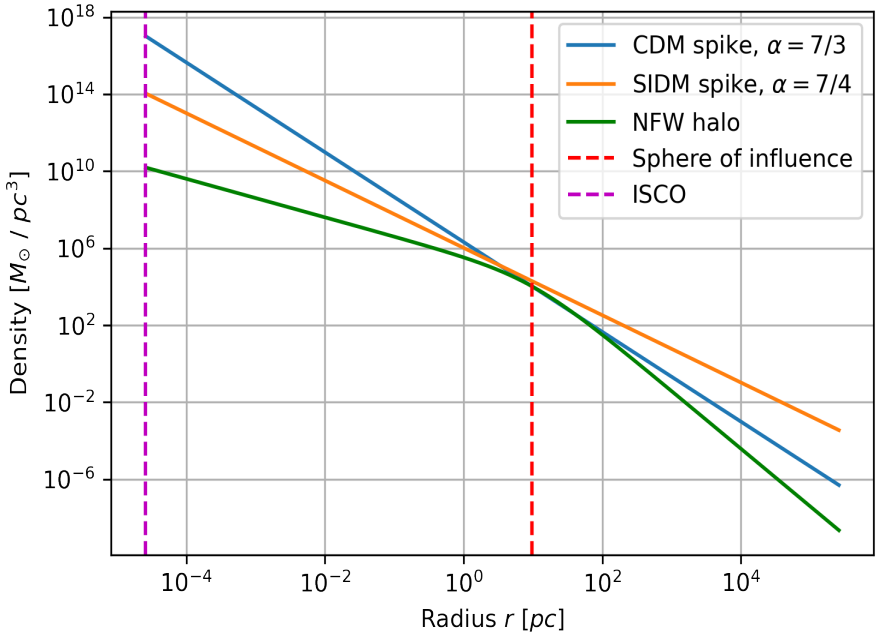

Fig. 2.3: The DM density is plotted as a function of the distance r from the SMBH. The green line represents an NFW halo with parameters $\{r_s, \rho_s\} = \{r_h, 4 \times 0.2^{\alpha_{CDM}}\,\rho_{sp,CDM}\}$. The parameters were selected such that the density function of CDM matches the NFW profile at the radius r_h of the sphere of influence (cf. Equation (2.1)), which is a continuity condition. r_h is indicated by a vertical red line. The blue line shows the CDM spike, and the orange line the SIDM spike. The ISCO is also marked in violet. The values of m_{BH} and σ are set to $9 \times 10^7 M_\odot$ and 200 km/s, respectively.

Additionally, there is still uncertainty about the temporal evolution of DM spikes around SMBHs. For example, mergers with smaller BHs or a SMBH that is experiencing adiabatic growth, which does not occur exactly at the center of its initial DM halo, can lead to the formation of a weaker cusp [29]. In the following, the changes in the DM density distribution around SMBHs due to these dynamical processes are not taken into account.

2.3 Orbital Evolution of Supermassive Black Hole Binaries

In this work, it is assumed that the two SMBHs of a SMBHB can be treated as point-like particles with masses m_1 and m_2 located at positions $\vec{r}_1$ and $\vec{r}_2$ within the framework of Newtonian approximation (*two-body problem*). The effects of GR become significant when the two SMBHs approach each other within a distance of $r_{ISCO,1}+r_{ISCO,2}$, where $r_{ISCO,i}$ represents the ISCO of the i-th SMBH. This is why the numerical calculation (see Chapter 3) of the SMBHB evolution is terminated when the separation becomes smaller than this value.

2.3.1 Keplerian Orbits

The Lagrangian function that describes the motion of the SMBHs on Keplerian orbits (neglecting dynamical friction and GW emission) is given by

$$L = T - V = \frac{m_1}{2}\dot{\vec{r}}_1^2 + \frac{m_2}{2}\dot{\vec{r}}_2^2 + G\,\frac{m_1 m_2}{|\vec{r}_1 - \vec{r}_2|}. \tag{2.8}$$

Due to the Galilean invariance of L, it is convenient to introduce center-of-mass (CoM) and relative coordinates:

$$\vec{R} = \frac{m_1\vec{r}_1 + m_2\vec{r}_2}{m_1 + m_2}, \qquad \vec{r} = \vec{r}_1 - \vec{r}_2. \tag{2.9}$$

Using the *reduced mass* $\mu = m_1 m_2/M$, where $M = m_1 + m_2$ is the *total mass*, the Lagrangian function in these coordinates can be expressed in the following form:

$$L = \frac{M}{2}\dot{\vec{R}}^2 + \frac{\mu}{2}\dot{\vec{r}}^2 + G\,\frac{m_1 m_2}{|\vec{r}|}. \tag{2.10}$$

The equations of motion for $\vec{R}$ and $\vec{r}$ can be obtained using the Euler-Lagrange formalism:

$$\ddot{\vec{R}} = \vec{0}, \qquad \ddot{\vec{r}} = \frac{\vec{F}_{Grav}(\vec{r})}{\mu} \qquad \text{with} \qquad \vec{F}_{Grav}(\vec{r}) = -G\,\frac{m_1 m_2}{|\vec{r}|^2}\,\frac{\vec{r}}{|\vec{r}|}. \tag{2.11}$$

By choosing the **CoM as the origin of the coordinate system**, i.e., $\vec{R} = \vec{0}$, and using polar coordinates $\vec{r} = (r\,\cos(\phi), r\,\sin(\phi), 0)$, the orbits of the two SMBHs can be described by

$$\vec{r}_1 = \frac{m_2}{M}\vec{r}, \qquad \vec{r}_2 = -\frac{m_1}{M}\vec{r} \qquad \text{with} \qquad \vec{r} = \frac{a(1-e^2)}{1 + e\,\cos(\phi)}\,\frac{\vec{r}}{r}, \tag{2.12}$$

where a is the semi-major axis, e the eccentricity and ϕ the eccentric anomaly of the elliptical orbits. The two-body motion is therefore planar. Using the conservation of energy and angular momentum, the magnitude of the total velocity can be derived. It is given by

$$v = |\dot{\vec{r}}| \overset{\vec{r}_1 \uparrow\downarrow \vec{r}_2}{=} |\dot{\vec{r}}_1| + |\dot{\vec{r}}_2| = v_1 + v_2 = \sqrt{GM\left(\frac{2}{r} - \frac{1}{a}\right)}. \tag{2.13}$$

From the above approach, the orbital angular frequency ω_{orb} and the angular momentum L_{orb} of the orbit can be obtained, and the formula for the total energy E_{orb} can be expressed in a more compact form, yielding

$$\omega_{orb} = \sqrt{\frac{GM}{a^3}} = 2\pi f_{orb} = \frac{2\pi}{T}, \tag{2.14}$$

$$L_{orb} = \mu r^2 \dot{\phi} = \mu\sqrt{GMa(1-e^2)} = \mu GM\sqrt{\frac{\mu(e^2-1)}{2E_{orb}}}, \tag{2.15}$$

$$E_{orb} = -\frac{Gm_1m_2}{2a}. \tag{2.16}$$

In Equation (2.14), T represents the period, and f_{orb} denotes the frequency of the orbital motion.

The dynamical friction resulting from the presence of DM (and baryonic matter), the hardening mechanism[8] via three-body-interactions with stars, and the emission of GWs during the inspiral are responsible for the gradual loss of energy and angular momentum in the binary system, causing the two SMBHs to approach each other over time. In this work, only the first and last effect play a role in the investigation of DM fingerprints in the GW signal of a SMBHB. The following two subsections describe these effects in detail. In Subsection 2.3.4, the resulting energy and angular momentum balance is established, and from that, the equations of motion for a and e are derived.

[8]Hardening mechanism: During this process, the orbits of the SMBHs become tighter through gravitational interactions with surrounding objects like stars, leading to a "hardening" of the system. For more details see, for example, [34].

2.3.2 Dynamical Friction

The initial phase of SMBHB evolution is primarily characterized by energy loss due to the gravitational interaction between DM and SMBHs, known as dynamical friction (DF) [35]. This phenomenon occurs when one SMBH moves through the matter halo of another, causing deceleration due to the increased matter density that forms behind that SMBH.
The interaction of DM particles in the overlap region of the spikes between the SMBHs is neglected, which is more consistent with the CDM model (cf. Subsection 2.1.1).

Static, non-relativistic DM spikes

In the following derivation of the formula for the DF caused by DM, it is assumed that a spherically symmetric and static (i.e., time-independent) DM spike has formed around each[9] SMBH, whose density can be described using Equation (2.3). The parameters of the two spikes can also differ from each other. In a first non-relativistic analysis, the DM spikes are assumed to move around the CoM in the same way as the SMBHs themselves. Thus, the proper motion of the DM particles relative to the corresponding SMBH is initially neglected. The mass ratio of the SMBHs and the initial eccentricity of their orbits can be chosen arbitrarily. In what follows, one SMBH is denoted as i and the other as j $(i, j = 1, 2;\ i \neq j)$.
Only the DM surrounding m_j has an influence on the motion of m_i, as at the location of m_i, the DM density of its own spike, according to Equation (2.3), is zero. Since for the mass m_{DM} of one DM particle surely $m_{DM} \gg m_1, m_2$ is valid, one can start with *Chandrasekhar's formula* for the change of velocity $\vec{v}_i$ of m_i by the DM of the spike around m_j based on [37]:

$$\frac{d\vec{v}_i}{dt} = 4\,\pi\,G^2\,m_i\,m_{DM}\,\ln(\Lambda)\int f(\vec{v}_{DM,j},\vec{r})\,\frac{\vec{v}_i - \vec{v}_{DM,j}}{|\vec{v}_i - \vec{v}_{DM,j}|^3}\,d^3v_{DM,j}. \tag{2.17}$$

Here, $\ln(\Lambda)$ represents the *Coulomb logarithm*, which will be discussed in more detail below. $\vec{v}_{DM,j}$ denotes the velocity of the DM particles, and $f(\vec{v}_{DM,j},\vec{r})$ represents the velocity distribution of these around m_i, which must satisfy the condition

$$\int f(\vec{v}_{DM,j},\vec{r})\,d^3v_{DM,j} = n_{DM,j}(\vec{r}), \tag{2.18}$$

[9] For example, in [36], a single stationary DM halo was assumed to surround the CoM of the SMBHB, in which both SMBHs orbit each other.

where $n_{DM,j}(\vec{r})$ stands for the DM number density, so that $\rho_{DM,j}(\vec{r}) = n_{DM,j}(\vec{r})\, m_{DM}$.
According to the above assumptions, which are visualized in Figure 2.4a, the velocity $\vec{v}_{DM,j}$ of the DM particles around m_i approximately corresponds to the velocity $\vec{v}_j$ of the j-th SMBH at each location. Thus, the velocity distribution can be written as

$$f(\vec{v}_{DM,j}, \vec{r}) = n_{DM,j}(\vec{r})\, \delta(\vec{v}_{DM,j} - \vec{v}_j). \tag{2.19}$$

By utilizing $\vec{v}_i \uparrow\downarrow \vec{v}_j$ (in the CoM frame, see Equation (2.12)), i.e., $\vec{v}_i = v_i\, \hat{\vec{v}}$ and $\vec{v}_j = -v_j\, \hat{\vec{v}}$ with $\hat{\vec{v}} = \frac{\vec{v}_i}{v_i}$, the following expression is obtained:

$$\frac{dv_i}{dt} \overset{(2.13)}{=} 4\,\pi\, G^2\, m_i\, \rho_{DM,j}(r)\, \ln(\Lambda)\, \frac{1}{v^2}. \tag{2.20}$$

Finally, the DF force $F_{DF,i}$ acting on m_i can be expressed as

$$F_{DF,i} = 4\,\pi\, G^2\, m_i^2\, \rho_{DM,j}(r)\, \ln(\Lambda)\, \frac{1}{v^2}. \tag{2.21}$$

The location, denoted as r, at which $\rho_{DM,j}(r)$ needs to be evaluated corresponds to the position of the i-th SMBH. In this context, there is no distinction between r as the distance to the j-th SMBH in $\rho_{DM,j}(r)$ and r as the separation between the i-th and j-th SMBH. This is due to the isotropy of the DM spike in the rest frame of the j-th SMBH and the fact that the two SMBHs always face each other (the line connecting them intersects the stationary CoM). In short, the DM density does not depend on the reference frame under the given non-relativistic conditions.

Rotating, non-relativistic DM spikes

Due to the gravitational interaction between a static DM spike and a SMBH, an increasing number of DM particles would fall into the SMBH over time, leading to a time-dependent density distribution of the spike during the inspiral. However, for short durations, the previous approximation can still be used.
In the plane where the evolution of the SMBHB takes place, a rotating DM disk with a spike-like density profile is now considered around each SMBH. In order for the DM particles to rotate on stable circular orbits around the j-th SMBH, the following condition applies to the

magnitude of their velocity $\vec{v}_{DM,j,rot}$ (in the rest frame of m_j):

$$v_{DM,j,rot} = \sqrt{\frac{G(m_j + m_{DM,j}(r))}{r}}, \tag{2.22}$$

where $m_{DM,j}(r)$ is the total mass of DM located within a sphere of radius r around m_j. According to Equation (2.5), for $r \ll r_h$, the approximation $m_j + m_{DM,j}(r) \approx m_j$ holds well.
The direction of rotation of the spikes around their respective SMBH usually corresponds to the direction of rotation of the SMBHB itself (see [38]). Each DM particle follows its SMBH, so it already has an intrinsic velocity $\vec{v}_{DM,j,intr}$ equal to the velocity $\vec{v}_j$ of the j-th SMBH. Additionally, there is the rotational velocity $\vec{v}_{DM,j,rot}$, which leads to a reduction of the total DM speed to an effective DM velocity $\vec{v}_{DM,j,eff}$ on the side of m_j where the other SMBH is located, as can be seen in Figure 2.4b. Thus, in the immediate vicinity of m_i applies: $\vec{v}_j \uparrow\downarrow \vec{v}_{DM,j,rot} \,||\, \vec{v}_i$. Hence, in general, it follows:

$$\vec{v}_{DM,j,eff} = \vec{v}_{DM,j,intr} + k\,\vec{v}_{DM,j,rot} = \left(-v_j + k\sqrt{\frac{Gm_j}{r}}\right)\hat{\vec{v}}, \tag{2.23}$$

with $\hat{\vec{v}} = \frac{\vec{v}_i}{v_i}$ and $k = \begin{cases} 0 & \rightarrow \text{ static spikes} \\ 1 & \rightarrow \text{ rotating spikes} \end{cases}$.

Instead of determining $f(\vec{v}_{DM,j}, \vec{r})$ at every location, it is sufficient to know the DM velocity distribution only in the vicinity of m_i [37]. Analogous to the above derivation, the more general form of the DF force acting on m_i as represented in Equation (2.21) can be derived, yielding

$$F_{DF,i} = 4\,\pi\,G^2\,m_i^2\,\rho_{DM,j}(r)\,\ln(\Lambda)\,\frac{1}{\left(v - k\sqrt{\frac{Gm_j}{r}}\right)^2}. \tag{2.24}$$

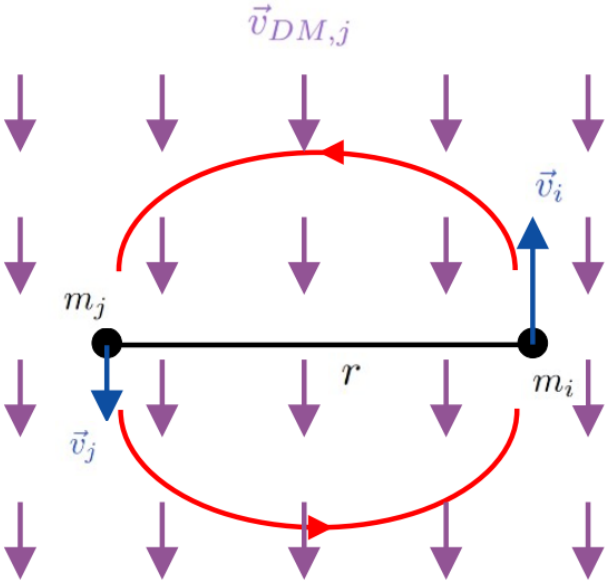

(a) Static, non-relativistic spikes.

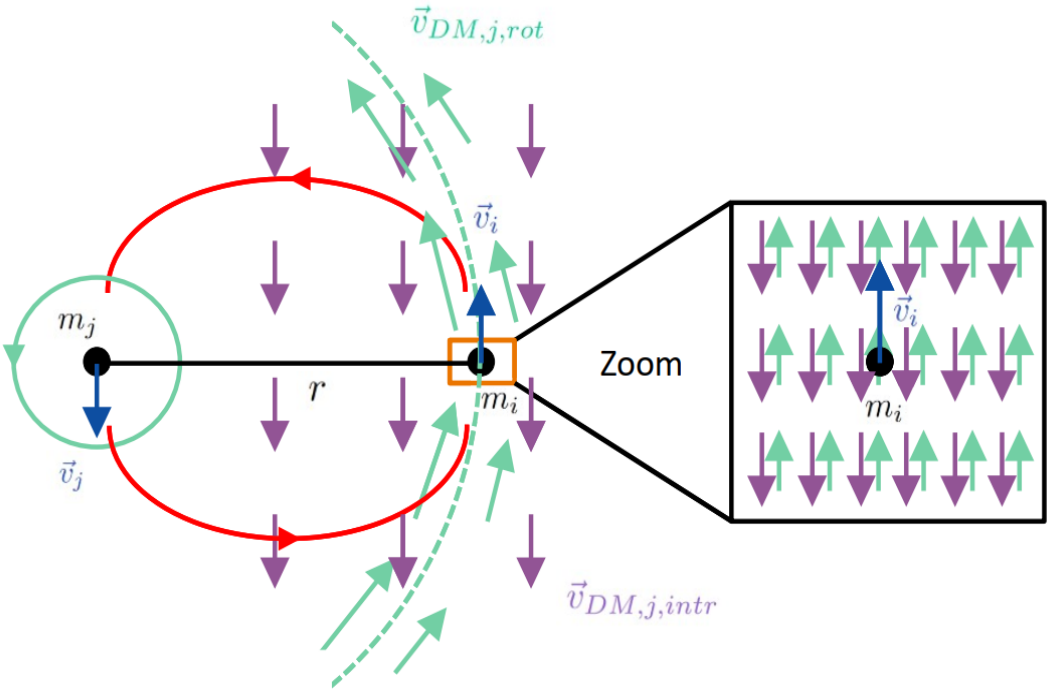

(b) Rotating, non-relativistic spikes.

Fig. 2.4: Shown are the differences between static and rotating spikes related to the velocity of DM particles within the spike around m_j near m_i. For clarity, the representation of the spike around m_i has been omitted. In both cases, non-relativistic conditions are assumed.

Total energy loss due to DF

Based on the previous considerations, the loss of energy over time by the SMBHB due to the DF mechanism can be obtained as follows:

$$\begin{aligned}\frac{dE_{DF}}{dt} &= \frac{dE_{DF,1}}{dt} + \frac{dE_{DF,2}}{dt} = -\left(F_{DF,1}\, v_1 + F_{DF,2}\, v_2\right) \\ &\overset{(2.12)}{=} -\underbrace{\left(F_{DF,1}\,\frac{m_2}{M} + F_{DF,2}\,\frac{m_1}{M}\right)}_{F_{DF}}\, v = -F_{DF}\, v.\end{aligned} \tag{2.25}$$

The following two specific cases are relevant for this work:

a) Static spikes ($k = 0$):

$$\begin{aligned}\frac{dE_{DF}}{dt} &\overset{(2.21)}{=} -4\,\pi\,G^2\,\ln(\Lambda)\,\frac{1}{v^2}\left(m_1^2\,\rho_{DM,2}(r)\,\frac{m_2}{M} + m_2^2\,\rho_{DM,1}(r)\,\frac{m_1}{M}\right)\, v \\ &= -\underbrace{4\,\pi\,G^2\,\ln(\Lambda)\,\frac{1}{v^2}\,\mu\left(m_1\,\rho_{DM,2}(r) + m_2\,\rho_{DM,1}(r)\right)}_{F^a_{DF}}\, v \\ &= -F^a_{DF}\, v.\end{aligned} \tag{2.26}$$

b) Rotating spikes ($k = 1$) and circular orbits ($e = 0$), i.e., $v = \sqrt{\frac{GM}{r}}$:

$$\begin{aligned}\frac{dE_{DF}}{dt} &\overset{(2.24)}{=} -4\,\pi\,G^2\,\ln(\Lambda)\left[m_1^2\,\rho_{DM,2}(r)\frac{1}{\left(v - \sqrt{\frac{Gm_2}{r}}\right)^2}\,\frac{m_2}{M} + m_2^2\,\rho_{DM,1}(r)\frac{1}{\left(v - \sqrt{\frac{Gm_1}{r}}\right)^2}\,\frac{m_1}{M}\right]\, v \\ &= -4\,\pi\,G^2\,\ln(\Lambda)\left[m_1^2\,\rho_{DM,2}(r)\frac{1}{\left[v\left(1 - \sqrt{\frac{m_2}{M}}\right)\right]^2}\,\frac{m_2}{M} + m_2^2\,\rho_{DM,1}(r)\frac{1}{\left[v\left(1 - \sqrt{\frac{m_1}{M}}\right)\right]^2}\,\frac{m_1}{M}\right]\, v \\ &= -\underbrace{4\,\pi\,G^2\,\ln(\Lambda)\,\frac{1}{v^2}\,\mu\left[m_1\,\rho_{DM,2}(r)\frac{1}{\left(1 - \sqrt{\frac{m_2}{M}}\right)^2} + m_2\,\rho_{DM,1}(r)\frac{1}{\left(1 - \sqrt{\frac{m_1}{M}}\right)^2}\right]}_{F^b_{DF}}\, v \\ &= -F^b_{DF}\, v.\end{aligned} \tag{2.27}$$

Estimation of the Coulomb logarithm

In general, the Coulomb logarithm $\ln(\Lambda)$ is given by the ratio of the maximum impact parameter $b_{\max}$ and the minimum impact parameter b_{min} [37]:

$$\ln(\Lambda) = \ln\left(\frac{b_{max}}{b_{min}}\right). \tag{2.28}$$

While for intermediate-mass ratio inspirals[10] (IMRIs), it is common to use $\Lambda = \sqrt{\frac{m_1}{m_2}} \gg 1$ with $m_1 \gg m_2$ [39], this definition is not applicable in the context of SMBHBs, as it would result in the DF disappearing for equal masses ($m_1 = m_2$: $\ln(\Lambda) = 0$). Therefore, an alternative way of estimating Λ is required.

The value of $b_{\max}$ is typically unknown a priori, but an estimation of its order of magnitude is often sufficient due to the extremely small slope of the logarithm for large arguments. For b_{min}, the impact parameter b_{90} is used, which indicates the distance at which particles are reflected at an angle of 90 degrees during their encounter with the SMBHs [40]. As mentioned in [37], b_{90} is chosen to be

$$b_{90} \approx \frac{GM}{v_{typ}^2} \approx \frac{GM}{\sigma^2} = r_h, \tag{2.29}$$

where the typical relative velocity v_{typ} of matter in the host galaxy of the SMBHB can be equated with the local velocity dispersion σ. Hence, b_{90} corresponds to the radius r_h of the sphere of influence of a SMBHB (cf. Equation (2.2)). Thus, finally follows:

$$\Lambda \approx \frac{b_{max}}{r_h} = \frac{b_{max}\,\sigma^2}{GM} \overset{!}{\gg} 1. \tag{2.30}$$

In the following, the effect on the DF in the case of relativistic velocities of the SMBHs is briefly discussed.

[10] IMRI: In such a system, a compact object with stellar mass (black hole or neutron star) undergoes an inspiral towards an intermediate-mass black hole with a mass ranging from 10^3 to $10^5 M_\odot$.

Relativistic correction to the DF formula

To motivate the relativistic correction to the DF formula, the maximum velocity of the SMBHs in a binary system can be estimated. Assuming equal-mass SMBHs ($m_1 = m_2 = m$) on circular orbits ($r = a$), and with the minimum distance between them given by $r_{min} = r_{ISCO,1} + r_{ISCO,2} = 12\,\frac{Gm}{c^2}$ (where the numerical computation of the SMBHB-code stops), the maximum total velocity v_{max} of the two SMBHs can be determined as the sum of their individual velocities v_1 and v_2 at $r = r_{min}$:

$$v_{max} = v(r_{min}) = v_1(r_{min}) + v_2(r_{min}) \overset{(2.13)}{=} \sqrt{\frac{2Gm}{r_{min}}} = \frac{\sqrt{6}}{6}\,c \approx 40.8\,\%\,c. \tag{2.31}$$

This corresponds to a relativistic velocity ($v_{max} > 10\,\%\,c$), underscoring the importance of considering the relativistic correction. However, the correction only plays a role in the final inspiral phase, as can be seen in Figure 2.5. For larger separations between the SMBHs, this effect can be neglected. The relativistic correction factor $\epsilon(v)$ is given by

$$\epsilon(v) = \gamma^2 \left[1 + \left(\frac{v}{c}\right)^2\right]^2 = \frac{\left[1 + \left(\frac{v}{c}\right)^2\right]^2}{1 - \left(\frac{v}{c}\right)^2}, \tag{2.32}$$

where γ represents the Lorentz factor [41]. This factor takes into account the increased deflection angle of the DM (considered as a fluid) as the orbiting SMBH traverses through it, while also accounting for the relativistic momentum of the fluid from the perspective of the SMBH [42].

According to [42], the correction to the total energy loss caused by DF due to interaction with DM can be expressed as

$$\left(\frac{dE_{DF}}{dt}\right)_{rel} = \epsilon(v)\,\left(\frac{dE_{DF}}{dt}\right)_{non\text{-}rel}. \tag{2.33}$$

Here, $\left(\frac{dE_{DF}}{dt}\right)_{non\text{-}rel}$ is equivalent to the expression in Equation (2.25).

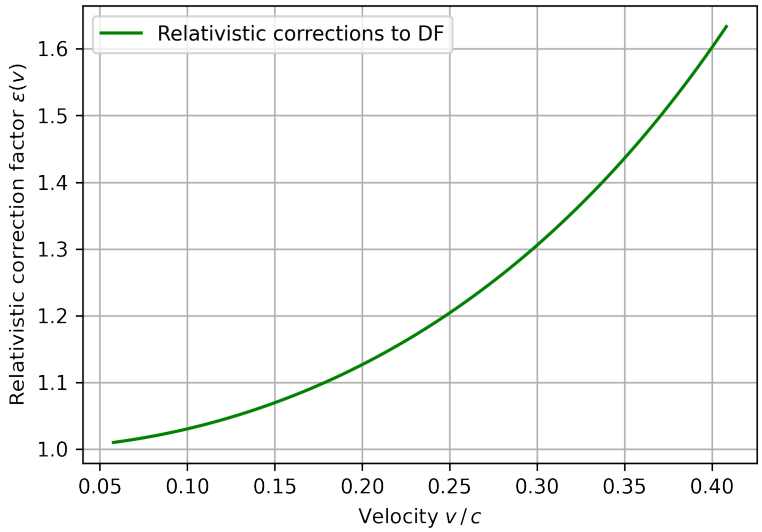

(a) Relativistic corrections to DF $\epsilon(v)$ as a function of the total velocity v in fractions of the speed of light c.

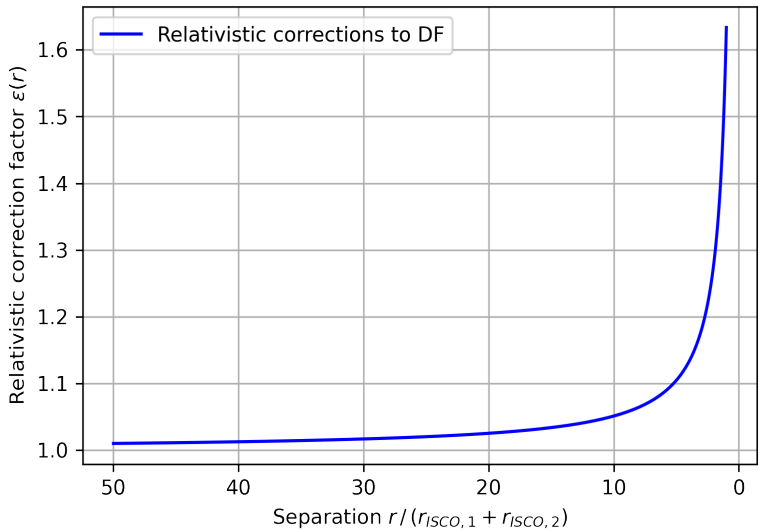

(b) Relativistic corrections to DF $\epsilon(r)$ as a function of the separation r between the SMBHs in fractions of $r_{ISCO,1} + r_{ISCO,2}$. v was replaced by $v(r) = \sqrt{\frac{2Gm}{r}}$ in Equation (2.32).

Fig. 2.5: The corrections to DF force due to relativistic effects in the final inspiral phase are depicted. Here, $m_1 = m_2 = m$ and circular orbits ($r = a$) were chosen.

2.3.3 Gravitational Wave Emission

In the final phase of the evolution of a SMBHB, the energy loss due to GW emission dominates over all other effects. The reason for this is that the DF force is proportional to v^{-2} (cf. Equation (2.21)), so the DF mechanism becomes negligible above a certain total velocity of the two SMBHs. This rapidly leads to their coalescence, which could be accompanied by a powerful burst of electromagnetic radiation, depending on local conditions such as matter density or magnetic field strength (*multi-messenger observation*) [43].
According to [44], the energy and angular momentum loss of the binary system because of GW radiation are described by

$$\left\langle \frac{dE_{GW}}{dt} \right\rangle = -\frac{32}{5}\frac{G^4\mu^2M^3}{c^5a^5}\frac{1}{(1-e^2)^{7/2}}\left(1+\frac{73}{24}e^2+\frac{37}{96}e^4\right), \tag{2.34}$$

$$\left\langle \frac{dL_{GW}}{dt} \right\rangle = -\frac{32}{5}\frac{G^{7/2}\mu^2M^{5/2}}{c^5a^{7/2}}\frac{1}{(1-e^2)^2}\left(1+\frac{7}{8}e^2\right). \tag{2.35}$$

In this case, the averaging $\langle ... \rangle$ has already been performed over an orbital period T, which will be explained in the next subsection.

2.3.4 Energy and Angular Momentum Balance

As shown in the previous subsections, the binary system loses energy and angular momentum through DF caused by the interaction with DM particles and the emission of GWs in the last phase of its evolution. Consequently, the SMBHs progressively approach each other until they finally merge. Thus, the energy and angular momentum balance of a single SMBHB can be formulated as follows:

$$\frac{dE_{orb}}{dt} = \left\langle \frac{dE_{DF}}{dt} \right\rangle + \left\langle \frac{dE_{GW}}{dt} \right\rangle, \tag{2.36}$$

$$\frac{dL_{orb}}{dt} = \left\langle \frac{dL_{DF}}{dt} \right\rangle + \left\langle \frac{dL_{GW}}{dt} \right\rangle. \tag{2.37}$$

Here, the terms on the right-hand side of the equations represent the averaging of energy and angular momentum over a period T (see Equation (2.14)), respectively, i.e.,

$$\langle (...) \rangle = \int_0^T \frac{dt}{T} (...) \,. \tag{2.38}$$

Averaging over a period is commonly used to obtain a more representative depiction of periodic motions. This enables the identification of general trends and facilitates better predictions regarding the behavior of a SMBHB. For a dissipative force such as the DF force, the temporal average can be transformed into an integral over ϕ according to [44]. It holds:

$$\begin{aligned} \left\langle \frac{dE_{DF}}{dt} \right\rangle &= \int_0^T \frac{dt}{T} \frac{dE_{DF}}{dt} = \left(1-e^2\right)^{3/2} \int_0^{2\pi} \frac{d\phi}{2\pi} \frac{dE_{DF}}{dt} \left(1+e\,\cos(\phi)\right)^{-2} \\ &\overset{(2.25)}{=} -\left(1-e^2\right)^{3/2} \int_0^{2\pi} \frac{d\phi}{2\pi} \frac{F_{DF}(r(\phi), v(\phi))\, v(\phi)}{\left(1+e\,\cos(\phi)\right)^2}, \end{aligned} \tag{2.39}$$

$$\begin{aligned} \left\langle \frac{dL_{DF}}{dt} \right\rangle &= \int_0^T \frac{dt}{T} \frac{dL_{DF}}{dt} \underset{[45]}{\overset{(*)}{=}} -\sqrt{GMa\left(1-e^2\right)} \int_0^T \frac{dt}{T} \frac{F_{DF}}{v} \\ &= -\sqrt{GMa}\,\left(1-e^2\right)^2 \int_0^{2\pi} \frac{d\phi}{2\pi} \frac{F_{DF}(r(\phi), v(\phi))}{\left(1+e\,\cos(\phi)\right)^2\, v(\phi)}. \end{aligned} \tag{2.40}$$

In the second step in Equation (2.40), marked by $(*)$, was used:

$$\begin{aligned} -\frac{dL_{DF}}{dt} &= -\left(\frac{dL_{DF,1}}{dt} + \frac{dL_{DF,2}}{dt}\right) = \left|\frac{d\vec{L}_{DF,1}}{dt}\right| + \left|\frac{d\vec{L}_{DF,2}}{dt}\right| \\ &= \left|\vec{r}_1 \times \vec{F}_{DF,1}\right| + \left|\vec{r}_2 \times \vec{F}_{DF,2}\right| = F_{DF,1} \left|-\vec{r}_1 \times \frac{\vec{v}_1}{v_1}\right| + F_{DF,2} \left|-\vec{r}_2 \times \frac{\vec{v}_2}{v_2}\right| \\ &\underset{(2.25)}{\overset{(2.12)}{=}} \underbrace{\left(F_{DF,1}\,\frac{m_2}{M} + F_{DF,2}\,\frac{m_1}{M}\right)}_{F_{DF}} \frac{1}{v} \left|\vec{r} \times \dot{\vec{r}}\right| \overset{\text{Ch. 2.3.1}}{=} \frac{F_{DF}}{v} \left|\left(r\,\hat{\vec{r}}\right) \times \left(\dot{r}\,\hat{\vec{r}} + r\,\dot{\phi}\,\hat{\vec{\phi}}\right)\right| \\ &= \frac{F_{DF}}{v}\, r^2\, \dot{\phi} \overset{(2.15)}{=} \sqrt{GMa\left(1-e^2\right)}\, \frac{F_{DF}}{v}, \end{aligned} \tag{2.41}$$

where $\hat{\vec{r}}$ and $\hat{\vec{\phi}}$ represent the unit basis vectors in polar coordinates. Furthermore, $\vec{F}_{DF,l} \uparrow\downarrow \vec{v}_l$, i.e., $\vec{F}_{DF,l} = -F_{DF,l}\,\frac{\vec{v}_l}{v_l}$, $l = 1, 2$, was utilized.

Now the coupled differential equations describing the secular evolution of the SMBHB parameters $e(t)$ and $a(t)$ can be formulated in a similar way as in [45]. These can be solved numerically using the SMBHB-code (cf. Chapter 3). The Equation (2.15) can also be written as

$$e = \sqrt{1 + \frac{2E_{orb}\, L_{orb}^2}{G^2 M^2 \mu^3}}. \tag{2.42}$$

Hence, the differential equation for $e(t)$ is given by

$$\begin{aligned} \frac{de}{dt} &\overset{(2.42)}{=} \frac{1}{2e}\, \frac{2}{G^2 M^2 \mu^3} \left(\frac{dE_{orb}}{dt}\, L_{orb}^2 + 2 L_{orb}\, E_{orb}\, \frac{dL_{orb}}{dt} \right) \\ &\overset{(2.15)}{=} \frac{e^2 - 1}{e} \left(\frac{dE_{orb}}{dt}\, \frac{1}{2E_{orb}} + 2 L_{orb}\, \frac{1}{2L_{orb}^2}\, \frac{dL_{orb}}{dt} \right) \\ &= \frac{e^2 - 1}{2e} \left(\frac{dE_{orb}}{dt}\, \frac{1}{E_{orb}} + 2\, \frac{dL_{orb}}{dt}\, \frac{1}{L_{orb}} \right). \end{aligned} \tag{2.43}$$

The temporal evolution of $a(t)$ can be described using

$$\frac{da}{dt} = \frac{dE_{orb}}{dt} \left(\frac{\partial E_{orb}}{\partial a} \right)^{-1}, \tag{2.44}$$

with $\frac{\partial E_{orb}}{\partial a} = \frac{G m_1 m_2}{2a^2}$ (cf. Equation (2.16)).

2.4 Gravitational Wave Signals of Individual SMBHBs

In this subsection, the mathematical derivation of GWs based on [44] will be outlined. For this purpose, the Einstein summation convention will be used. As mentioned in the introduction of this bachelor thesis, GWs are solutions of the linearized Einstein field equations (EFEs). The EFEs are known to be

$$R_{\mu\nu} - \frac{1}{2} R\, g_{\mu\nu} = \frac{8\pi G}{c^4} T_{\mu\nu}. \tag{2.45}$$

Here, $R_{\mu\nu}$ represents the Ricci tensor, R the Ricci scalar, $g_{\mu\nu}$ is the metric tensor, and $T_{\mu\nu}$ the energy–momentum tensor of matter.
The starting point is the consideration of a small perturbation $h_{\mu\nu}$ of the flat-space metric $\eta_{\mu\nu}$ known from Special Relativity, i.e.,

$$g_{\mu\nu} = \eta_{\mu\nu} + h_{\mu\nu} \qquad \text{with} \qquad |h_{\mu\nu}| \ll 1. \tag{2.46}$$

Next, the left-hand side of (2.45) is extended to linear order in $h_{\mu\nu}$, so that the linearized Einstein field equations,

$$\Box \bar{h}_{\mu\nu} + \eta_{\mu\nu}\partial^\rho\partial^\sigma \bar{h}_{\rho\sigma} - \partial^\rho\partial_\nu \bar{h}_{\mu\rho} - \partial^\rho\partial_\mu \bar{h}_{\nu\rho} = -\frac{16\pi G}{c^4} T_{\mu\nu}, \tag{2.47}$$

are obtained, with $\bar{h}_{\mu\nu} = h_{\mu\nu} - \frac{1}{2}\eta_{\mu\nu}\eta^{\alpha\beta}h_{\alpha\beta}$ and the flat space d'Alembertian $\Box = \partial^\alpha\partial_\alpha = \frac{1}{c^2}\frac{\partial^2}{\partial t^2} - \Delta$, which implies that GWs travels at the speed of light c. To reach the form of a simple inhomogeneous wave equation for $\bar{h}_{\mu\nu}$,

$$\Box \bar{h}_{\mu\nu} = -\frac{16\pi G}{c^4} T_{\mu\nu}, \tag{2.48}$$

one uses the gauge freedom in GR and choose the *Lorentz gauge*,

$$\partial^\nu \bar{h}_{\mu\nu} = 0. \tag{2.49}$$

The GWs emitted by various sources propagate through the vacuum on their path to the detectors. Therefore, a more detailed discussion of the solution of Equation (2.48) for $T_{\mu\nu} = 0$ is now required.

The *transverse-traceless (TT) gauge*, along with another condition (see [44]), reduces the degrees of freedom of the symmetric tensor $h_{\mu\nu}$ from ten to two. The solutions of $\Box\bar{h}_{\mu\nu} = 0$ are plane waves. It follows:

$$h^{TT}_{\mu\nu} = e_{\mu\nu}(\vec{k})\, e^{ik^\lambda x_\lambda}. \tag{2.50}$$

Here, $e_{\mu\nu}(\vec{k})$ represents the polarization tensor and $k^\mu = (\omega/c, \vec{k})$ the wave four-vector with the spatial wave vector $\vec{k}$ ($|\vec{k}| = \omega/c$) and the angular frequency ω of the GW. x^μ denotes the known space-time four-vector with $x^\mu = (ct, \vec{x})$. In addition, $x_\mu = \eta_{\mu\nu}x^\nu = (ct, -\vec{x})$.
For example, the non-vanishing components of the real part of $h^{TT}_{\mu\nu}$ for a GW propagating in the z-direction can be expressed as

$$h^{TT}_{ab} = \begin{pmatrix} h_+ & h_\times \\ h_\times & -h_+ \end{pmatrix} \cos\left[\omega\left(t - \frac{z}{c}\right)\right], \tag{2.51}$$

where h_+ and $h_\times$ are the two independent polarization modes of the GW, and $a, b = 1, 2$ are indices in the transverse (x, y) plane.
According to [44], [31] and [46][11], for **circular orbits**[12], the gravitational waveform of a binary system like an individual SMBHB is described by the following equations:

$$h_+(t) = \frac{1}{D_0}\,\frac{4\,G\,\mu\,\omega^2_{orb}(t)\,r^2(t)}{c^4}\,\frac{1+\cos^2(\iota)}{2}\,\cos\left[\Phi(t)\right], \tag{2.52}$$

$$h_\times(t) = \frac{1}{D_0}\,\frac{4\,G\,\mu\,\omega^2_{orb}(t)\,r^2(t)}{c^4}\,\cos(\iota)\,\sin\left[\Phi(t)\right], \tag{2.53}$$

$$\Phi(t) = \int_{t_0}^{t} \omega(t')\,dt'. \tag{2.54}$$

D_0 represents the luminosity distance to the considered system at the time of GW emission, $\Phi(t)$ the phase of the GW and ι is the inclination angle as the angle between the line-of-sight and the rotation axis of the binary. Furthermore, ω corresponds to twice the angular frequency ω_{orb} of the binary system, i.e., $\omega = 2\,\omega_{orb}$ [31].

[11] This reference examines the special case of SMBHBs, already taking into account the redshift (see below).
[12] For elliptical orbits, the corresponding equations are significantly more complex (see, for example, [44]), and are therefore not considered in this work.

As mentioned earlier, the system loses energy through various effects, causing the orbital radii of the SMBHs to change over time. However, it is common to assume that this process occurs adiabatically, allowing for the approximation of quasi-circular orbits at any time [31].
The *strain* $h(t)$ caused by passing GWs and measured by a GW detector can be expressed as a linear combination of the polarization modes:

$$h(t) = F_+ h_+(t) + F_\times h_\times(t), \tag{2.55}$$

where $F_{+,\times}$ are the detector pattern functions that depend in general on the GW frequency f and the location of the binary system in the sky [47].
To facilitate discussions on detectability and parameter accuracy in GW observations, it is advantageous to work in the frequency domain. According to [31], the corresponding Fourier transformation is given by

$$\tilde{h}(f) = \int_{-\infty}^{\infty} h(t)\, e^{2\pi i f t}\, dt. \tag{2.56}$$

For simplicity, in the next subsection, it is assumed that the GWs arrive at the detector in such a way that the $\times$ mode vanishes, meaning it is optimally aligned for the $+$ mode. This is the case, for example, when $\iota = \pi/2$. Thus, due to $F_+ = 1$ and $F_\times = 0$ [31], it follows that $h(t) = h_+(t) = A(t)\, \cos[\Phi(t)]$ with

$$A(t) = \frac{1}{D_0}\, \frac{4\, G\, \mu\, \omega_{orb}^2(t)\, r^2(t)}{c^4}\, \frac{1 + \cos^2(\iota)}{2}. \tag{2.57}$$

In the frequency range of interest, the amplitude $A(t)$ of the GW varies slowly, while the phase $\Phi(t)$ changes rapidly. As a result, the Fourier transformation of the gravitational waveform can be approximated using the *stationary phase method*. This method involves neglecting the rapidly oscillating term and considering only the slowly oscillating term [31]. Consequently, the gravitational waveform $\tilde{h}(f)$ in the Fourier domain based on [31] is given by

$$\tilde{h}(f) = \frac{1}{2}\, e^{i\Psi(t)}\, A(t) \sqrt{\frac{2\pi}{\ddot{\Phi}(t)}}, \tag{2.58}$$

with

$$\Psi(t) = 2\pi f \left(t_c + \frac{D_0}{c} - t \right) + \Phi(t) - \Phi_c - \frac{\pi}{4}, \tag{2.59}$$

where Φ_c is the GW phase at and t_c the time of coalescence.
Finally, the dimensionless *characteristic strain* h_c can be defined as

$$h_c(f) = 2\, f \, \left| \tilde{h}(f) \right| \overset{(2.58)}{\underset{(2.54)}{=}} A(t)\, f \sqrt{\frac{2\pi}{\dot{\omega}}} = A(t) \sqrt{\frac{f^2}{\dot{f}}}. \tag{2.60}$$

For Chapter 4.2, the signal-to-noise ratio SNR will also play an important role. It is given by

$$\mathrm{SNR}^2 = \int_{-\infty}^{\infty} d(\ln(f)) \left[\frac{h_c(f)}{h_n(f)} \right]^2 \qquad \text{with} \qquad h_n(f) = \sqrt{f\, S_n(f)}, \tag{2.61}$$

where $h_n(f)$ is the noise amplitude and $S_n(f)$ the spectral noise density which depends on the GW detector [6], [48].

Accounting for cosmic expansion

So far, the effect of the Hubble expansion of the universe on the GW signal has not been taken into account because nearby binaries were assumed. However, this consideration can be relevant when dealing with SMBHBs, since they are likely to be the strongest GW sources and detectors are therefore sensitive to them over larger distances, i.e., cosmological distances. To get an understanding of the distances involved, the parameter z is introduced, which represents the redshift of the GW signal. It indicates that the sources of GWs typically are moving away from earth. The resulting luminosity distance D is given by

$$D = (1 + z)\, D_0, \tag{2.62}$$

where D_0 was defined below Equation (2.54).
The time and GW frequency in the rest frame of the source (t, f) are related to those in the reference frame where the detector is located (t_{obs}, f_{obs}), according to [44], as follows:

$$t_{obs} = (1 + z)\, t \qquad \text{and} \qquad f_{obs} = \frac{f}{1 + z}. \tag{2.63}$$

This leads to the following expression for $A(f_{obs})$ from Equation (2.57):

$$\begin{aligned} A(f_{obs}) &\overset{(**)}{=} \frac{(1+z)}{D}\,\frac{4\,G\,\mu}{c^4}\,\left(f_{obs}\,(1+z)\,\pi\right)^2\,\left[\frac{GM}{\left(f_{obs}\,(1+z)\,\pi\right)^2}\right]^{2/3}\,\frac{1+\cos^2(\iota)}{2} \\ &= \frac{1}{D}\,\frac{4\,(1+z)^{5/3}}{c^4}\,(G\mathcal{M})^{5/3}\,(\pi f_{obs})^{2/3}\,\frac{1+\cos^2(\iota)}{2}. \end{aligned} \tag{2.64}$$

Here, the *chirp mass*[13] $\mathcal{M} = \mu^{3/5}M^{2/5}$ has been introduced. Furthermore, for $(**)$ was used:

$$f_{obs} = \frac{1}{1+z}\,\frac{2\omega_{orb}}{2\pi} \overset{(2.14)}{\underset{r=a}{=}} \frac{1}{1+z}\,\frac{1}{\pi}\sqrt{\frac{GM}{r^3}} \qquad \Leftrightarrow \qquad r = \left[\frac{GM}{\left(f_{obs}\,(1+z)\,\pi\right)^2}\right]^{1/3}. \tag{2.65}$$

2.5 Dark Matter Density as a Function of the Characteristic Strain h_c

In this subsection, an expression for the density profile $\rho_{DM}(r)$ of the DM around the SMBHs will be derived as a function of the observed GW frequency f_{obs} and the measured characteristic strain $h_c(f_{obs})$. This formula will play an important role in Chapter 4.3.

For this purpose, the following assumptions are made:

- For simplicity, the orbits of m_1 and m_2 are circular, i.e., $e = 0$ and $r = a$.
- The two SMBHs have equal masses: $m_1 = m_2 = m$, so that $\rho_{DM,1}(r) = \rho_{DM,2}(r) = \rho_{DM}(r)$ can be assumed.
- There is only energy loss due to non-relativistic DF and GW emission.
- GWs coming in the detector from the optimal direction for the + mode, i.e., $h(t) = h_+(t)$.

First, $\dot{\omega}$ in Equation (2.60) can be replaced by

$$\dot{\omega} = \frac{\partial\omega}{\partial r}\,\frac{dr}{dt}, \tag{2.66}$$

with

[13] The chirp mass $\mathcal{M}$ is often introduced because it is easier to measure than the individual masses of the components of a binary system.

$$\frac{\partial \omega}{\partial r} = 2\,\frac{\partial \omega_{orb}}{\partial r} \overset{(2.14)}{=} -3\sqrt{\frac{2Gm}{r^5}}, \tag{2.67}$$

$$\begin{aligned}
\frac{dr}{dt} &\overset{(2.44)}{=} \frac{dE_{orb}}{dt}\left(\frac{\partial E_{orb}}{\partial r}\right)^{-1} \overset{(2.36)}{=} \Bigg[\underbrace{\left\langle \frac{dE_{DF}}{dt}\right\rangle}_{=\frac{dE_{DF}}{dt}} + \left\langle \frac{dE_{GW}}{dt}\right\rangle\Bigg]\left(\frac{\partial E_{orb}}{\partial r}\right)^{-1} \\
&\overset{(2.27)}{\underset{(2.34)}{=}} -\left[4\,\pi\,G^2\,\ln(\Lambda)\,\frac{1}{v}\,\mu\,\frac{2\,m\,\rho_{DM}(r)}{\left(1-k\,\frac{\sqrt{2}}{2}\right)^2} + \frac{32}{5}\frac{G^4\mu^2M^3}{c^5r^5}\right]\left(\frac{\partial E_{orb}}{\partial r}\right)^{-1} \\
&\overset{(2.13)}{\underset{(2.16)}{=}} -\left[2\,\sqrt{2}\,\pi\,G^{3/2}\,\ln(\Lambda)\,m^{3/2}\,r^{1/2}\,\frac{\rho_{DM}(r)}{\left(1-k\,\frac{\sqrt{2}}{2}\right)^2} + \frac{64}{5}\frac{G^4m^5}{c^5r^5}\right]\frac{2r^2}{Gm^2} \\
&= -\left[4\,\sqrt{2}\,\pi\,G^{1/2}\,\ln(\Lambda)\,m^{-1/2}\,r^{5/2}\,\frac{\rho_{DM}(r)}{\left(1-k\,\frac{\sqrt{2}}{2}\right)^2} + \frac{128}{5}\frac{G^3m^3}{c^5r^3}\right].
\end{aligned} \tag{2.68}$$

Substituting the two expressions into Equation (2.66) leads to

$$\dot{\omega} = 24\,\pi\,G\,\ln(\Lambda)\,\frac{\rho_{DM}(r)}{\left(1-k\,\frac{\sqrt{2}}{2}\right)^2} + \frac{384}{5}\sqrt{2}\,\frac{G^{7/2}\,m^{7/2}}{c^5\,r^{11/2}}. \tag{2.69}$$

For the characteristic strain $h_c(f_{obs})$ from Equation (2.60), the expression is now

$$\begin{aligned}
h_c^2(f_{obs})\,\dot{\omega} &\overset{(2.63)}{=} A^2(f_{obs})\,(1+z)^2\,f_{obs}^2\,2\,\pi \\
&\overset{(2.64)}{=} \left[\frac{1}{D}\,\frac{4\,(1+z)^{5/3}}{c^4}\,(G\mathcal{M})^{5/3}\,(\pi f_{obs})^{2/3}\,\frac{1+\cos^2(\iota)}{2}\right]^2 (1+z)^2\,f_{obs}^2\,2\,\pi \\
&= 2^{7/3}\,\pi^{7/3}\,\frac{1}{D^2}\,\frac{(1+z)^{16/3}}{c^8}\,G^{10/3}\,m^{10/3}\,f_{obs}^{10/3}\left(1+\cos^2(\iota)\right)^2.
\end{aligned} \tag{2.70}$$

This is equivalent to

$$24\,\pi\,h_c^2(f_{obs})\,G\,\ln(\Lambda)\,\frac{\rho_{DM}(f_{obs},h_c(f_{obs}))}{\left(1-k\,\frac{\sqrt{2}}{2}\right)^2} =$$

$$= 2^{7/3}\,\pi^{7/3}\,\frac{1}{D^2}\,\frac{(1+z)^{16/3}}{c^8}\,G^{10/3}\,m^{10/3}\,f_{obs}^{10/3}\left(1+\cos^2(\iota)\right)^2 - \frac{384}{5}\sqrt{2}\,h_c^2(f_{obs})\,\frac{G^{7/2}\,m^{7/2}}{c^5\,r^{11/2}}$$

$$\overset{(2.65)}{=} \frac{(2\,\pi)^{7/3}}{D^2}\,\frac{(1+z)^{16/3}\,(G\,m\,f_{obs})^{10/3}}{c^8}\,\left(1+\cos^2(\iota)\right)^2 - \frac{384}{5}\sqrt{2}\,h_c^2(f_{obs})\,\frac{(G\,m)^{7/2}}{c^5}\,\left[\frac{(f_{obs}\,(1+z)\,\pi)^2}{2Gm}\right]^{11/6}$$

$$= \frac{(2\,\pi)^{7/3}}{D^2}\,\frac{(1+z)^{16/3}\,(G\,m\,f_{obs})^{10/3}}{c^8}\,\left(1+\cos^2(\iota)\right)^2 - \frac{3}{5}\,2^{17/3}\,\pi^{11/3}\,h_c^2(f_{obs})\,\frac{(G\,m)^{5/3}}{c^5}\,\left(f_{obs}\,(1+z)\right)^{11/3}.$$

Rearranging the equation to $\rho_{DM}(f_{obs},h_c(f_{obs}))$ finally gives

$$\rho_{DM}(f_{obs},h_c(f_{obs})) = \frac{\left(1-k\,\frac{\sqrt{2}}{2}\right)^2}{\ln(\Lambda)}\left[\frac{1}{3}\,2^{-2/3}\,\pi^{4/3}\,\frac{1}{D^2}\,\frac{(1+z)^{16/3}\,G^{7/3}\,(m\,f_{obs})^{10/3}}{c^8\,h_c^2(f_{obs})}\,\left(1+\cos^2(\iota)\right)^2\right.$$

$$\left.-\frac{1}{5}\,(2\,\pi)^{8/3}\,\frac{G^{2/3}\,m^{5/3}}{c^5}\,\left(f_{obs}\,(1+z)\right)^{11/3}\right],$$

$$\rho_{DM}(f_{obs},h_c(f_{obs})) = \mathcal{A}\,\frac{f_{obs}^{10/3}}{h_c^2(f_{obs})} - \mathcal{B}\,f_{obs}^{11/3}, \tag{2.71}$$

with

$$\mathcal{A} = \frac{1}{3}\,\frac{1}{2^{2/3}}\,\frac{\left(1-k\,\frac{\sqrt{2}}{2}\right)^2}{\ln(\Lambda)}\,\frac{1}{D^2\,c^8}\,\left(\pi^4\,(1+z)^{16}\,G^7\,m^{10}\right)^{1/3}\,\left(1+\cos^2(\iota)\right)^2, \tag{2.72}$$

$$\mathcal{B} = \frac{1}{5}\,2^{8/3}\,\frac{\left(1-k\,\frac{\sqrt{2}}{2}\right)^2}{\ln(\Lambda)}\,\frac{1}{c^5}\,\left(\pi^8\,(1+z)^{11}\,G^2\,m^5\right)^{1/3}. \tag{2.73}$$

Here, $\mathcal{A}$ and $\mathcal{B}$ depend only on the SMBHB parameters k, D, z, m, ι and Λ (cf. Equation (2.30)), which could be determined separately by, for example, multi-messenger observations.

3 SMBHB-Code

The SMBHB-code is an extension of the IMRI-code, developed by me, for the study of SMBHBs. The IMRI-code (`https://github.com/DMGW-Goethe/imripy`) was written by my colleague Niklas Becker. Accordingly, the SMBHB-code can produce the same results as the IMRI-code under the conditions of an IMRI. It is capable of numerically calculating the time evolution of the orbital parameters $e(t)$ and $a(t)$ for the inspiral of SMBHs as well as the form of the GWs emitted by these systems. In this process, the components of binary systems can lose energy due to various effects such as DF when the SMBHs are passing through DM spikes. The code uses geometrized units with $G = c = 1$ and converts each occurring unit to parsecs (pc) before using it. It is freely available on GitHub (`https://github.com/DMGW-Goethe/SMBHBpy`). The code can be tested within the Jupyter Notebook *BasicExamples.ipynb*.

3.1 Necessary Adjustments of the IMRI-Code

An IMRI is the inspiral of a stellar-mass object and an intermediate-mass black hole (IMBH) with a mass ranging from 10^3 to $10^5 M_\odot$. In this scenario, the lighter component of the binary system moves through the DM halo of the IMBH, resulting in a gradual approach through the emission of GWs and the DF mechanism. Because of the large mass ratio between the two components it is typically assumed that the IMBH rests at the CoM of the system. This is not the case for SMBHBs. In these systems, both SMBHs move around their common CoM and both may have a DM halo surrounding them.

The class *SystemProp*, which describes the properties of the binary system, has been extended to include additional parameters such as a second DM halo and the radius r_h of the sphere of influence, as well as the maximum impact parameter b_{max} for calculating the Coulomb logarithm $\ln(\Lambda)$. An overview of all important code parameters can be found in the next subsection. Furthermore, the formula for the DF force in the class *DynamicalFriction* had to be replaced by the one derived in Subsection 2.3.2.

3.2 Overview of the most Important Code Parameters

The following table contains all important parameters of the SMBHB-code.

Symbol (code)	Symbol (this work)	Equation	Definition
m1	m_1		Mass of the first SMBH
m2	m_2		Mass of the second SMBH
D_luminosity	D	(2.62)	Luminosity distance
sigma	σ		Velocity dispersion of the host bulge
b_max	b_{max}		Maximum impact parameter
ln_Lambda	$\ln(\Lambda)$	(2.28)	Coulomb logarithm
inclination_angle	ι		Inclination angle
relCovFactor	$\epsilon(v)$	(2.32)	Relativistic correction factor to DF
k	k	(2.23)	$k = 0$: static spikes; $k = 1$: rotating spikes ($e \stackrel{!}{=} 0$)
r_isco_i	$r_{ISCO,i}$	(2.7)	ISCO of the i-th SMBH
r_infl	r_h	(2.2)	Influence radius of the binary
m_reduced	μ		Reduced mass
m_total	M		Total mass
z	z		Redshift parameter
r_sp_i	$r_{sp,i}$		Parameter for the DM spike size
rho_sp_i	$\rho_{sp,i}$	(2.6)	Normalization density
alpha_i	α_i	(2.4)	Slope of the DM spike
R0	r_0		Initial separation for circular orbits
R_fin, a_fin	$r_{ISCO,1} + r_{ISCO,2}$	(2.7)	Final condition for the evolution
a0	a_0		Initial major semi-axis of the orbits
e0	e_0		Initial eccentricity of the SMBHB

Tab. 3.1: Overview of the most important parameters used in the code.

4 Results

In this chapter the results of this work will be presented and discussed. First, the influence of different orbital parameters and masses of the SMBHs on the evolution of the SMBHB and the form of the emitted GWs is investigated in more detail. In this context, the distinctions between the results for CDM and SIDM spikes become apparent. Rotating spikes and the effect of including relativistic corrections to the DF will also be considered as possible factors influencing the motion of the SMBHs. The second subsection will be dedicated to Cassini's limitations in the detectability of GW signals. This allows to set limits on the masses of the SMBHs and their distances within which a detection of GWs is possible by the Cassini spacecraft. Finally, using the Cassini data as an example, a method will be presented to obtain the DM distribution around the SMBHs of a binary system.

4.1 Impact of Various System Parameters on the Orbital Evolution of SMBHBs

To obtain the results presented in this subsection, the values listed in Table 4.1 for the respective parameters are always used.

D	σ	b_{max}	ι	$r_0 = a_0$
65 Mpc	200 km/s	10 kpc	$\pi/2$	$50\,(r_{ISCO,1} + r_{ISCO,2})$

Tab. 4.1: Table with the values used for individual parameters.

The choice of the value for D of 65 Mpc will become more significant later on. 200 km/s is a typical value for the velocity dispersion σ in elliptic galaxies [49]. b_{max} was chosen such that $\Lambda \gg 1$ holds (cf. Equation (2.30)). As mentioned in a previous subsection, an estimation of the order of magnitude of b_{max} is sufficient. The inclination angle ι was chosen to be $\pi/2$, so that $h(t) = h_+(t)$ (cf. Chapter 2.4). r_0 was selected such that $f_{obs}(r_0)$ is on the order of 10^{-7} Hz to 10^{-5} Hz.

In the following, the temporal evolution of the separation r and the semi-major axis a, respectively, the dependence between e and a and the form of the GWs will be plotted for two different SMBHBs with equal-mass SMBHs. Accordingly, for $\alpha_1 = \alpha_2$: $\rho_{DM,1}(r) = \rho_{DM,2}(r) = \rho_{DM}(r)$.

4.1.1 Results for $m_1 = m_2 = 10^6\, M_\odot$

First, the findings for $m_1 = m_2 = 10^6\, M_\odot$ are discussed.

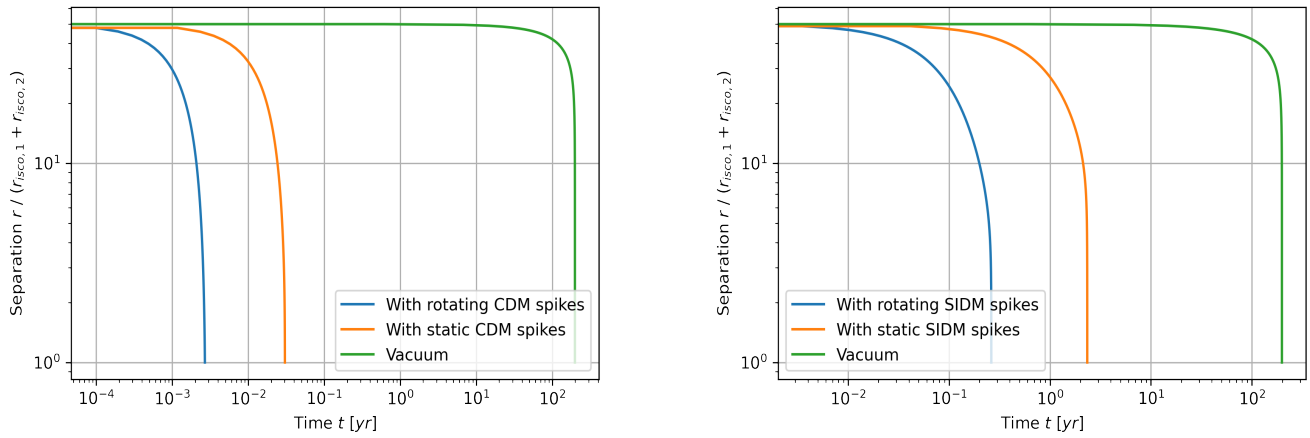

Fig. 4.1: Temporal evolution of the separation r for CDM spikes (left) und SIDM spikes (right) for circular orbits. The blue line is the result for rotating, non-relativistic spikes and the orange for static, non-relativistic spikes. The case where the SMBHB loses energy only through GW emission, i.e., the situation without DM clouds (vacuum), is represented by the green line.

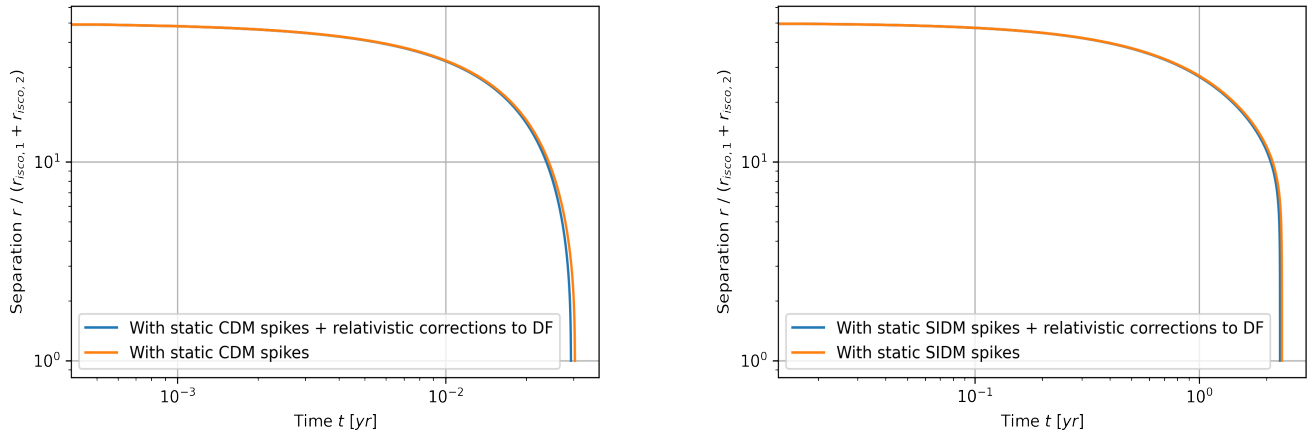

Fig. 4.2: Temporal evolution of the separation r for CDM spikes (left) und SIDM spikes (right) for circular orbits. The blue line is the result for static spikes with relativistic corrections to the DF and the orange for static, non-relativistic spikes from Figure 4.1.

The results reflect exactly the theoretical predictions from Chapter 2: the larger the decelerating DF force F_{DF}, the shorter the time until the two SMBHs merge. For rotating spikes, according to Subsection 2.3.2, F_{DF} is larger by a factor of $\left(1 - \frac{\sqrt{2}}{2}\right)^{-2} \approx 11.66$ than for static spikes. By including relativistic effects the DF force is larger by a factor of about 1 to 1.63 (cf. Figure 2.5).

As a consequence, the evolution of the SMBHB proceeds faster in both cases. Furthermore, F_{DF} is also proportional to the DM spike density. For this reason, CDM spikes - compared to SIDM spikes - have the same shortening effect on the time to coalescence (see Figure 2.3). In addition, the beginning of the final phase of evolution, i.e., when GW emission starts to dominate energy loss, is clearly visible: from this point onwards, the magnitude of the rate of change of separation increases significantly.

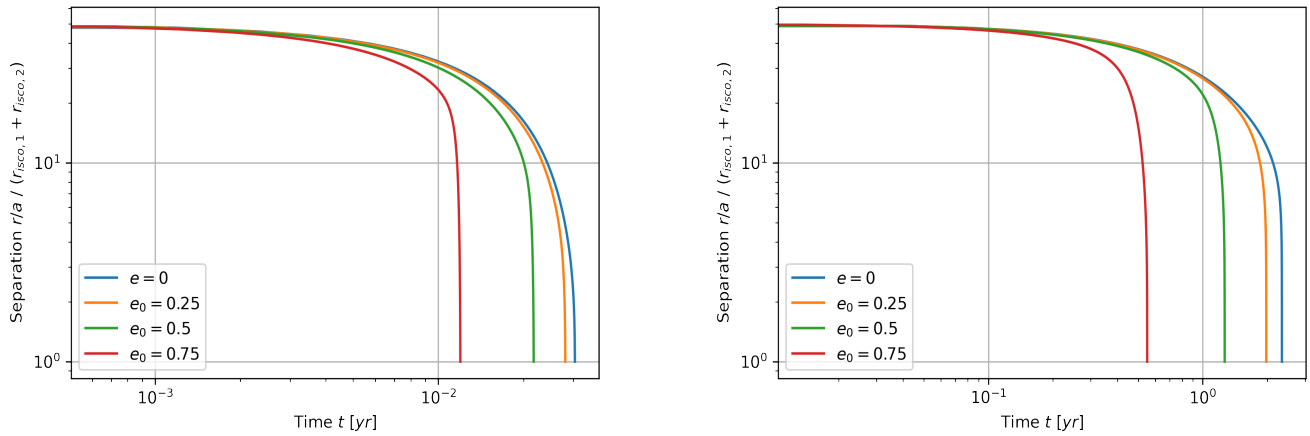

Fig. 4.3: Temporal evolution of the separation r for $e_0 = e(t) = 0$ and of the semi-major axis a for $e_0 \neq 0$ in the case of static, non-relativistic CDM spikes (left) und static, non-relativistic SIDM spikes (right). The different colors represent different initial values e_0 of eccentricity.

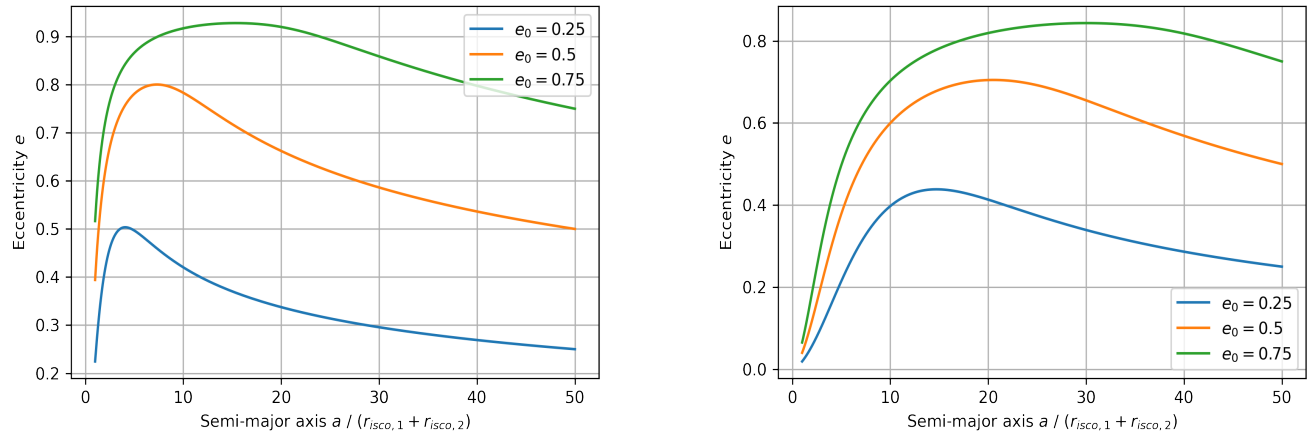

Fig. 4.4: Evolution of the eccentricity e depending on the semi-major axis a for different e_0 in the case of static, non-relativistic CDM spikes (left) and static, non-relativistic SIDM spikes (right). The different colors represent different initial values e_0 of eccentricity.

As depicted in Figure 4.3, in both cases a higher initial eccentricity e_0 leads to a similar reduction in the lifetime of the binary system. As it was shown in [45], the DF force, characterized by $F_{DF} \sim r^{-\alpha} v^{-2}$ with $\alpha < 3$ (slope of the DM spikes), leads to an eccentrification ($de/dt > 0$) of the SMBH orbits. On the other hand, the emission of GWs results in circularization ($de/dt < 0$). Thus, the evolution can be clearly divided into the phases explained in Chapter 2.3: once the value of the semi-major axis a falls below a certain value, the energy loss due to GW emission dominates over the interaction with DM particles through DF.

Furthermore, in Figure 4.4 it can be seen that in the case of SIDM spikes (right), e converges to approximately zero during the course of evolution for all considered initial values e_0. This behavior is not seen for CDM spikes (left). In the latter case, the eccentricity converges to different final values for various e_0. In addition, the maximum change of e compared to the initial value e_0 is larger for CDM than for SIDM. This is due to the higher DM density around the SMBHs in the CDM model, which leads to a stronger DF force and a longer-lasting effect of eccentrification, i.e., up to a smaller a. As a result, the time in the final phase is not sufficient to completely circularize the different orbits.

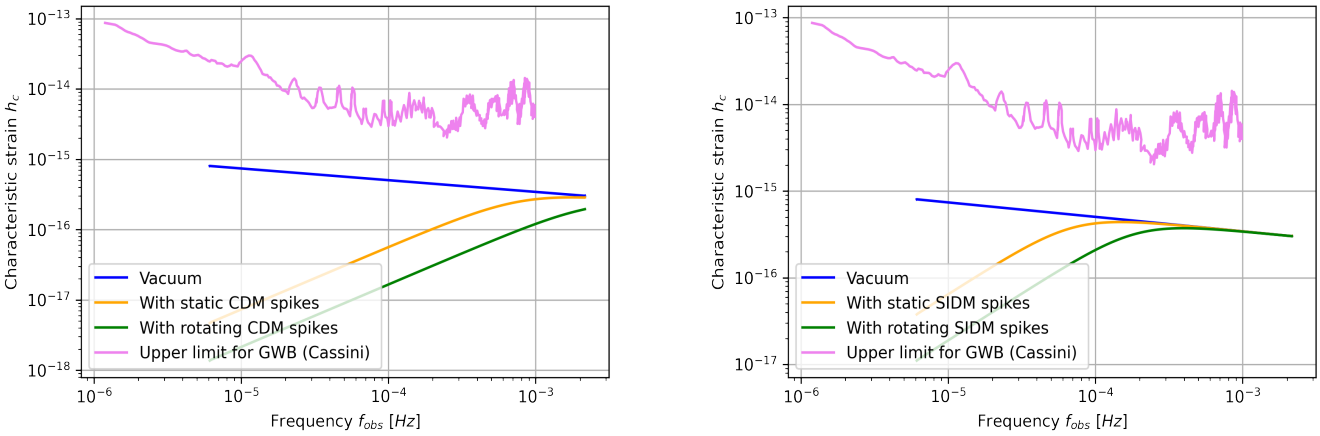

Fig. 4.5: The GW spectrum of the SMBHB is shown in the case of static, non-relativistic DM spikes (orange) and rotating, non-relativistic DM spikes (green) for circular orbits. Again, a distinction is made between CDM (left) and SIDM (right). Additionally, the situation without DM spikes (vacuum) is represented in blue, and the upper limit on the GWB (from Cassini) during its first observation period is shown in pink.

By comparing the GW spectra with and without DM spikes, it can be clearly seen that above a certain frequency (or distance according to Equation (2.65)) the transition between the two phases mentioned earlier occurs also for circular orbits. For the regime where the energy and

angular momentum loss due to DF dominates, $h_c \sim f_{obs}^{(5-\alpha)/3}$ holds. The final phase, where GW emission dominates, is characterized by $h_c \sim f_{obs}^{-1/6}$. These proportionalities are obtained using the Equations (2.65), (2.69), and (2.70). The values for h_c in the DF regime for rotating, non-relativistic spikes ($k = 1$) are smaller by a factor of $\left(1 - \frac{\sqrt{2}}{2}\right)$ than these for static, non-relativistic spikes ($k = 0$) (see Chapter 2.5).

For higher frequencies, especially in the case of SIDM, the characteristic strain h_c cannot be distinguished from that of the vacuum case anymore. Therefore, h_c does not contain any information about the environment of the SMBHs. In the CDM model, a difference between the two GW spectra (with and without DM) is observed up to the frequency corresponding to $r = r_{ISCO,1} + r_{ISCO,2}$ (here, the numerical calculation stops). This is due to the higher density of DM in the inner region of the spikes compared to the SIDM model. This leaves more distinct fingerprints of DM in the characteristic strain even at higher f_{obs}.

4.1.2 Results for $m_1 = m_2 = 10^8\, M_\odot$

Since the explanations for the following plots are the same as for those in the above case ($m_1 = m_2 = 10^6\, M_\odot$), only the significant differences related to the masses of the SMBHs are discussed below the figures.

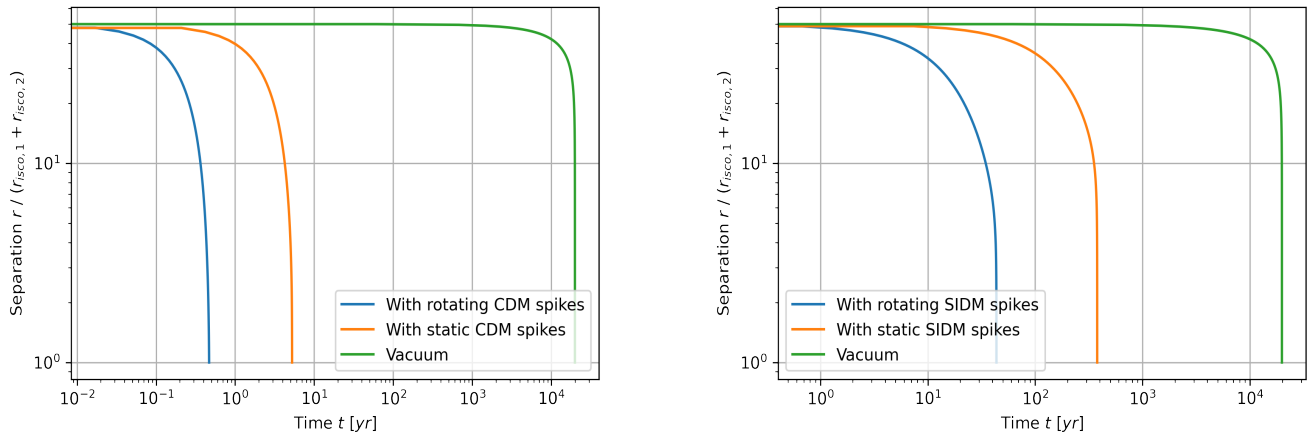

Fig. 4.6: Temporal evolution of the separation r for CDM spikes (left) und SIDM spikes (right) for circular orbits. The blue line is the result for rotating, non-relativistic spikes and the orange for static, non-relativistic spikes. The case where the SMBHB loses energy only through GW emission, i.e., the situation without DM clouds (vacuum), is represented by the green line.

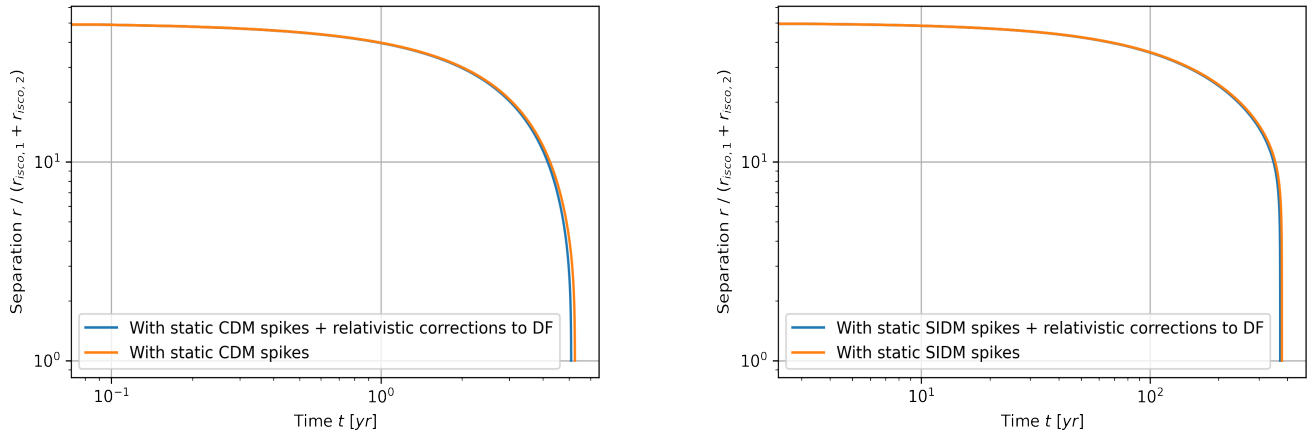

Fig. 4.7: Temporal evolution of the separation r for CDM spikes (left) und SIDM spikes (right) for circular orbits. The blue line is the result for static spikes with relativistic corrections to the DF and the orange for static, non-relativistic spikes from Figure 4.6.

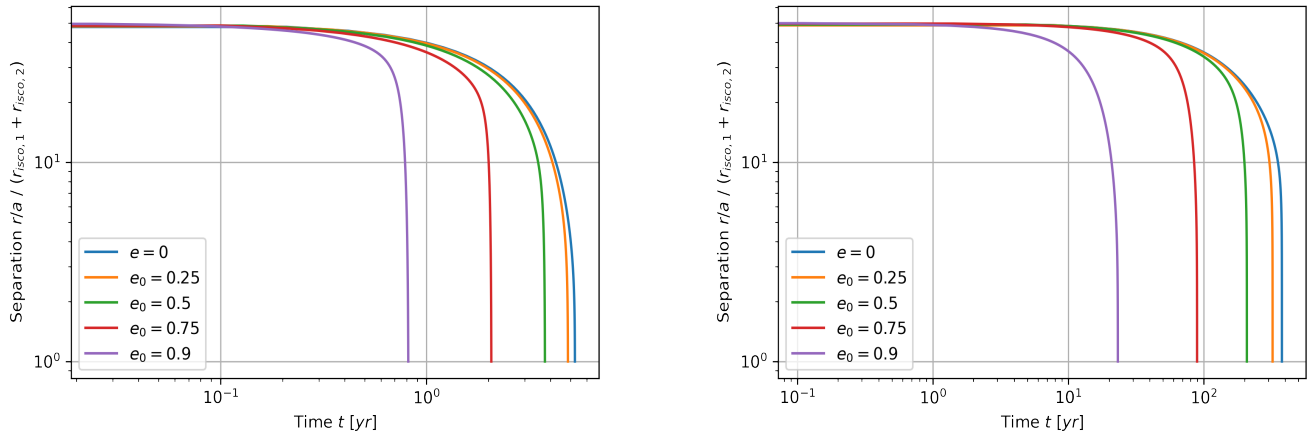

Fig. 4.8: Temporal evolution of the separation r for $e_0 = e(t) = 0$ and of the semi-major axis a for $e_0 \neq 0$ in the case of static, non-relativistic CDM spikes (left) und static, non-relativistic SIDM spikes (right). The different colors represent different initial values e_0 of eccentricity.

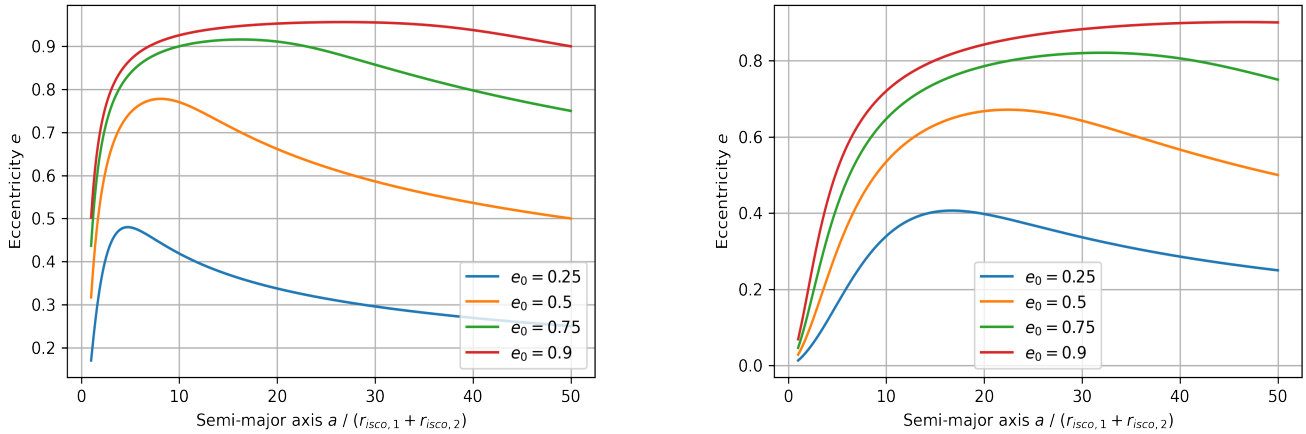

Fig. 4.9: Evolution of the eccentricity e depending on the semi-major axis a for different e_0 in the case of static, non-relativistic CDM spikes (left) and static, non-relativistic SIDM spikes (right).The different colors represent different initial values e_0 of eccentricity.

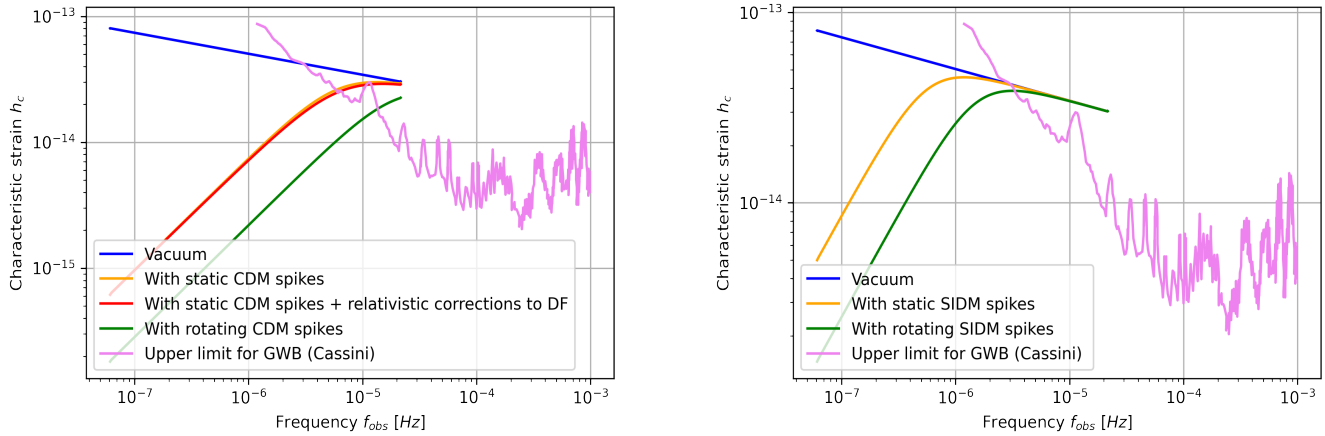

Fig. 4.10: The GW spectrum of the SMBHB is shown in the case of static, non-relativistic DM spikes (orange) and rotating, non-relativistic DM spikes (green) for circular orbits. Again, a distinction is made between CDM (left) and SIDM (right). For CDM, the result for static spikes with relativistic corrections to DF is also plotted in red, as in this case it still slightly differs from the one without these corrections. Additionally, the situation without DM spikes (vacuum) is represented in blue, and the upper limit on the GWB (from Cassini) is shown in pink.

At first glance, one might assume that the larger masses of SMBHs would extend the time to coalescence by about two orders of magnitude. However, this conclusion is not entirely correct as the increase in masses by a factor of 100 simultaneously leads to an increase in the initial separation r_0 by the same factor according to Equation (2.7). Furthermore, the increase in masses and r_0 results in a decrease in the orbital frequency f_{orb} (cf. Equation (2.14)) and,

consequently, the observed frequency f_{obs} of the emitted GWs. As a consequence, the inspiral is shifted further into Cassini's frequency range. Moreover, for the masses larger by a factor of 100, one obtains an increase of the characteristic strain h_c by approximately two orders of magnitude in both cases (CDM and SIDM).

4.2 Cassini's Limitations in the Detectability of Gravitational Wave Signals

As mentioned in the motivation of this study, the phase of the SMBHB evolution where the separation between the two SMBHs rapidly decreases occurs in Cassini's frequency range. This is evident from the GW spectra in conjunction with the temporal evolution of r or a presented in the previous subsections.

The authors of [50] found that the main contribution to the total strain amplitude of the GWB comes from SMBH coalescence events occurring at redshifts $0 < z < 1$. This supports the assumption used in the following analysis that a part of the GWB (from Cassini) could originate from an individual nearby SMBHB, whose GW signal is characterized by a high characteristic strain. This assumption is crucial since it has not yet been possible to extract signals from the GWB that could be attributed to individual sources. Furthermore, there is still uncertainty about the astrophysical or cosmological events that generate this background.

Firstly, one has to examine the requirements for such an individual SMBHB so that its GWs could be detected by Cassini. One important quantity that constrains both the maximum distance of the binary and the possible range of SMBH masses is the signal-to-noise ratio (SNR). In Figure 4.11[14], the SNR[15] is plotted as a function of the *initial frequency* f_{ini} and the chirp mass of the system for $m_1 = m_2$ in the upper panel and for $m_2/m_1 = 0.01$ in the lower panel. The SNR is calculated for the Virgo Cluster, which is located at a distance of $D = 17\,\mathrm{Mpc}$ [51]. In this context, f_{ini} is defined as the frequency of the GW signal at the beginning of Cassini's observation period.

The idea is to calculate f_{ini} for different $\mathcal{M}$ and then examine for which chirp masses the corresponding SNR from Figure 4.11 takes the highest values. This allows to constrain the mentioned mass range. Furthermore, only possible equal-mass SMBHBs in the Virgo Cluster

[14] While the SNR in this figure is plotted for Cassini's third observation time, I assume that it is approximately equivalent to that of the first measurement.

[15] It is important to note that the SNR was estimated for various combinations of f_{ini} and $\mathcal{M}$ prior to the measurements. Therefore, it can be considered as an independent quantity for constraining the values of $m_1 = m_2 = m$ and D of the SMBHBs.

are considered for this purpose. For larger distances than $D = 17\,\mathrm{Mpc}$ or for a mass ratio different from unity, the SNR decreases further. From Figure 4.11, it is also evident that the SNR increases with increasing initial frequency for a fixed $\mathcal{M}$. Although this behavior is only seen up to a certain maximum value for f_{ini}, this is not relevant as this value is not reached by a SMBHB. It is also clear that f_{ini} is larger when the separation between the SMBHs is already smaller. For this reason, I decided to coincide the timing of the SMBHs' coalescence with the end of Cassini's 40-day observation period. Therefore, I assume that the two SMBHs reach the separation at which the numerical calculation terminates, i.e., $r = r_{ISCO,1} + r_{ISCO,2}$, 35 days after the start of Cassini's measurement. After that, the two SMBHs have an additional 5 days[16] until their merger. This approach allows to achieve the highest possible initial frequency for a fixed chirp mass defined by

$$f_{ini} \overset{(2.65)}{=} \frac{1}{(1+z)\,\pi}\sqrt{\frac{G\,M}{\left[N\,(r_{ISCO,1}+r_{ISCO,2})\right]^3}}, \tag{4.1}$$

where N can be numerically determined using the SMBHB-code by

$$35\,\mathrm{days} \approx \underbrace{t(r_{ISCO,1}+r_{ISCO,2})}_{\text{total evolution time}} - t(N(r_{ISCO,1}+r_{ISCO,2})). \tag{4.2}$$

Another reason for this assumption is that the SMBHB has the highest rate of change in separation r during the last 40 days before coalescence, as discussed in the previous subsection. Therefore, a large distance is "sampled" by the SMBHs within the observation time of Cassini. Consequently, in the next subsection, it can be calculated the DM density around a SMBH for the largest possible spatial area.

The following table presents different values of $\mathcal{M}$ along with their corresponding N, f_{ini}, and the resulting SNR read from Figure 4.11. These values are also indicated in red in the same figure. For smaller or larger values of the chirp mass than these, the frequency range considered in this figure for f_{ini} is not sufficient to read the SNR. However, these are not necessary, as will become clear later. Based on the discussion in the previous subsection regarding GW spectra, I have chosen to focus on the case of static, non-relativistic CDM spikes and circular orbits.

[16] This is a conservative estimate for the time to coalescence using $t_{coal} = \frac{5}{256}\,\frac{c^5}{G^3}\,\frac{(r_{ISCO,1}+r_{ISCO,2})^4}{M^2\mu}$ from [44] for circular orbits in the case where a SMBHB loses energy only through GW emission, which is applicable in the final phase.

$m_1 = m_2\,[M_\odot]$	$\mathcal{M}\,[M_\odot]$	N	$f_{ini}\,[\mathrm{Hz}]$	SNR (fig. 4.11)
10^7	8.71×10^6	12.3	5.06×10^{-6}	0 to 1
2×10^7	1.74×10^7	6.65	6.37×10^{-6}	0 to 1
3×10^7	2.61×10^7	5.0	6.51×10^{-6}	1 to 5
4×10^7	3.48×10^7	4.2	6.34×10^{-6}	1 to 5
5×10^7	4.35×10^7	3.73	6.06×10^{-6}	1 to 5
6×10^7	5.22×10^7	3.41	5.78×10^{-6}	1 to 5
7×10^7	6.09×10^7	3.18	5.50×10^{-6}	≈ 5
8×10^7	6.96×10^7	3.0	5.23×10^{-6}	5 to 10
9×10^7	7.83×10^7	2.87	4.99×10^{-6}	5 to 10
10^8	8.71×10^7	2.75	4.79×10^{-6}	5 to 10

Tab. 4.2: SNR for different values of $\mathcal{M}$ and f_{ini}. $\{D,\, \sigma,\, b_{max}\} = \{17\,\mathrm{Mpc},\, 200\,\mathrm{km/s},\, 10\,\mathrm{kpc}\}$.

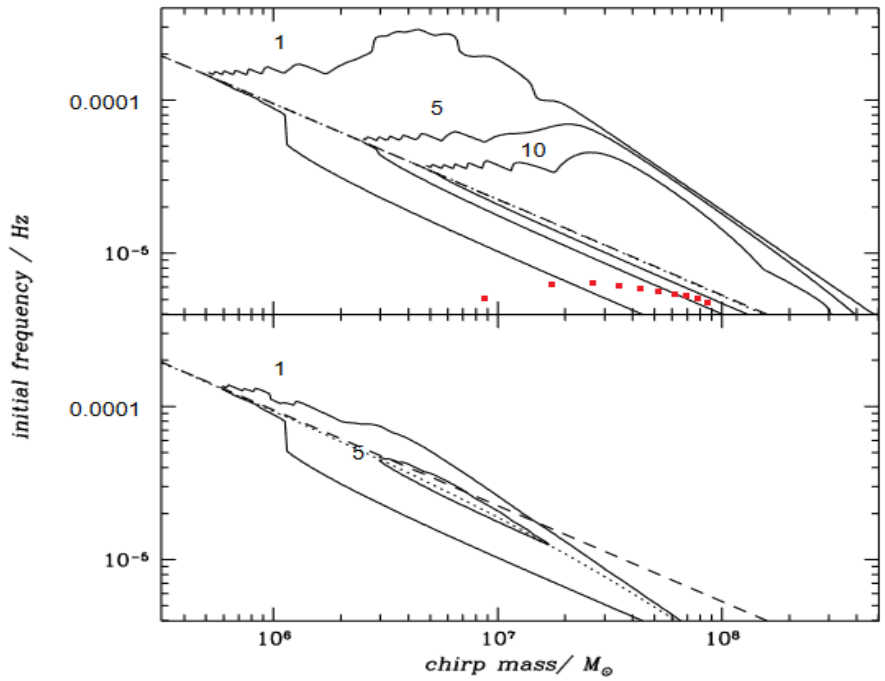

Fig. 4.11: The figure illustrates the detectable inspiral signals emitted by SMBHBs in the Virgo Cluster ($D = 17\,\mathrm{Mpc}$). The contour plots depict the levels of 1, 5, and 10 for the SNR in the $(\mathcal{M}, f_{ini})$-plane. The values listed in Table 4.2 are also marked in red. The top panel corresponds to the case of $m_1 = m_2$, while the bottom panel represents the case of $m_2/m_1 = 0.01$. The meaning of the dashed diagonal line and the dotted line is irrelevant in this work [15].

From Table 4.2 and Figure 4.11, the mass range with the highest SNR ($\gtrsim 5$) can be determined to be $7 \times 10^7\, M_\odot \leq m \leq 10^8\, M_\odot$ with $m_1 = m_2 = m$. The maximum distance reachable by the spacecraft is estimated to be 100 Mpc in [51]. Therefore, the range of the luminosity distance for SMBHBs used in the following is $17\,\text{Mpc} \leq D \leq 100\,\text{Mpc}$. Within these intervals, an upper and lower bound for the GW spectrum of an individual SMBHB can now be calculated. These two limit cases are shown in the next two subfigures.

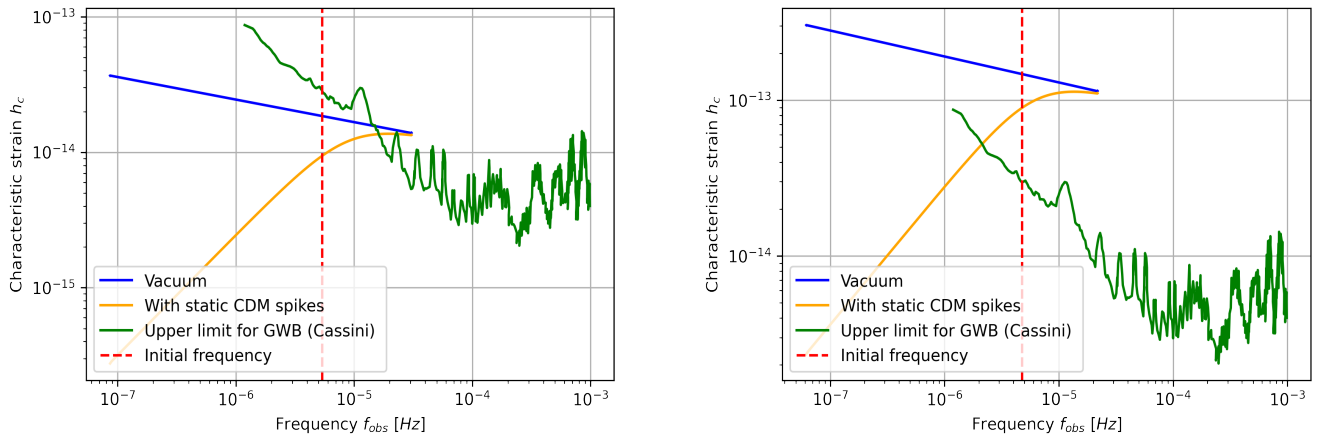

(a) Lower bound for the GW spectrum. $\{D,\, m\} = \{100\,\text{Mpc},\, 7 \times 10^7\, M_\odot\}$.

(b) Upper bound for the GW spectrum. $\{D,\, m\} = \{17\,\text{Mpc},\, 10^8\, M_\odot\}$.

Fig. 4.12: The GW spectrum is depicted for the two limit cases in the scenario of static, non-relativistic CDM spikes and circular orbits. f_{ini} is marked with a vertical red line. In addition, the vacuum case is also considered. $\{\sigma,\, b_{max}\,,\, \iota,\, r_0\} = \{200\,\text{km/s},\, 10\,\text{kpc},\, \pi/2,\, 50\,(r_{ISCO,1} + r_{ISCO,2})\}$

In the following, a combination of D and m needs to be found whose h_c best matches a part of the GWB within the detectable frequency range ($f_{max} = f_{obs}(r = r_{ISCO,1} + r_{ISCO,2}) \geq f_{obs} \geq f_{ini}$) for the case of static, non-relativistic CDM spikes. Since, as mentioned above, this part is assumed to be dominated by the GW signal from this individual nearby SMBHB.
By calculating the total absolute deviation $\Delta = \sum_{f_{obs}=f_{ini}}^{f_{max}} |h_{c,Cassini}(f_{obs}) - h_{c,SMBHB}(f_{obs})|$ for each detectable combination of D and m, I conclude that approximately $D = 65\,\text{Mpc}$ and $m = 9 \times 10^7\, M_\odot$ is the most appropriate choice[17] (see Figure 4.13). In this context, $h_{c,Cassini}$ represents the upper limit on the characteristic strain from Cassini, and $h_{c,SMBHB}$ the

[17]For this combination $\Delta \approx 0.7 \times 10^{-12}$ for 100 different values of $f_{obs} \in [f_{ini}, f_{max}]$ is valid. The larger the number of values used for f_{obs}, the larger Δ becomes. The maximum number is limited by the accuracy of the SMBHB-code in calculating $h_{c,SMBHB}$.

characteristic strain of the GW signal from the respective SMBHB for static, non-relativistic CDM spikes. For $m \geq 2 \times 10^8\, M_\odot$ the characteristic strain of the signal is too high for all possible values of D.

I would also like to mention that there are combinations for which the total absolute deviation fits slightly better. However, for these combinations, the calculated DM density distributions by using Cassini data (see next subsection) are quite unphysical: within the detectable frequency range, they are highly discontinuous and take negative values for certain f_{obs}. Therefore, I have discarded these combinations.

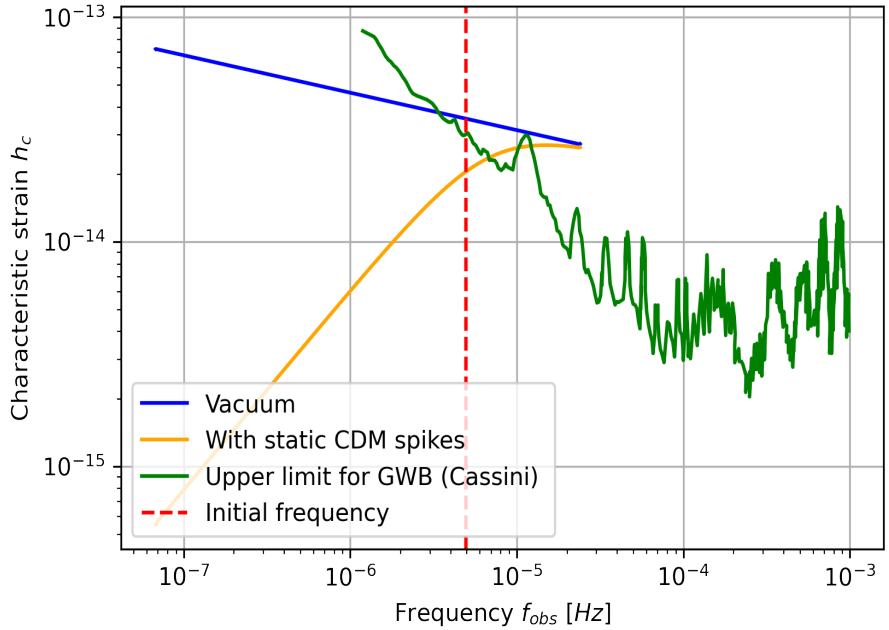

Fig. 4.13: GW spectrum for the appropriate values of D and m. In addition, the vertical red line marks the initial frequency f_{ini}. $\{D,\, m,\, \sigma,\, b_{max}\,,\, \iota,\, r_0\} = \{65\,\text{Mpc},\, 9 \times 10^7\, M_\odot,\, 200\,\text{km/s},\, 10\,\text{kpc},\, \pi/2,\, 50\,(r_{ISCO,1} + r_{ISCO,2})\}$.

Interestingly, Cassini was also sensitive to GW signals from extreme mass ratio inspirals (EMRIs) from compact objects with masses $\gtrsim 30\, M_\odot$ and the SMBH Sgr A* of our galaxy [51]. However, the radius of the orbit around the galactic center of such light objects, even in the final phase of their evolution, changes very little within Cassini's observation period. Therefore, their f_{ini} is only minimally smaller than $f_{obs}(r_{ISCO,1} + r_{ISCO,2})$. As a result, EMRIs potentially detected by Cassini are not suitable for the analysis in this work.

4.3 Calculation of the Dark Matter Density around SMBHs using Cassini Data

Finally, in this subsection, a lower limit for the DM density ρ_{DM} is determined based on the upper limit on the GWB, characterized by the characteristic strain $h_{c,\,Cassini}$. The parameters of the SMBHB whose characteristic strain best matches $h_{c,\,Cassini}$, as shown in Figure 4.13, are used to calculate $\mathcal{A}$ and $\mathcal{B}$ in Equation (2.71). For $h_c(f_{obs})$, $h_{c,Cassini}(f_{obs})$ is utilized in this formula. In Figure 4.14, the DM density obtained from the Cassini data is compared with the density distribution of the corresponding CDM and SIDM spike. The values of r_{sp} and ρ_{sp} for both DM spikes are calculated by using the SMBH mass ($m = 9 \times 10^7\, M_\odot$) of the selected SMBHB and Equations (2.2) and (2.6), respectively.

It should be noted that, of course, only the range between "35 days to ISCO1+2" and "ISCO1+2 (stop numerical calculation)" can be considered for the subsequent discussion of the plot. This frequency range is referred to as "relevant" in the following.

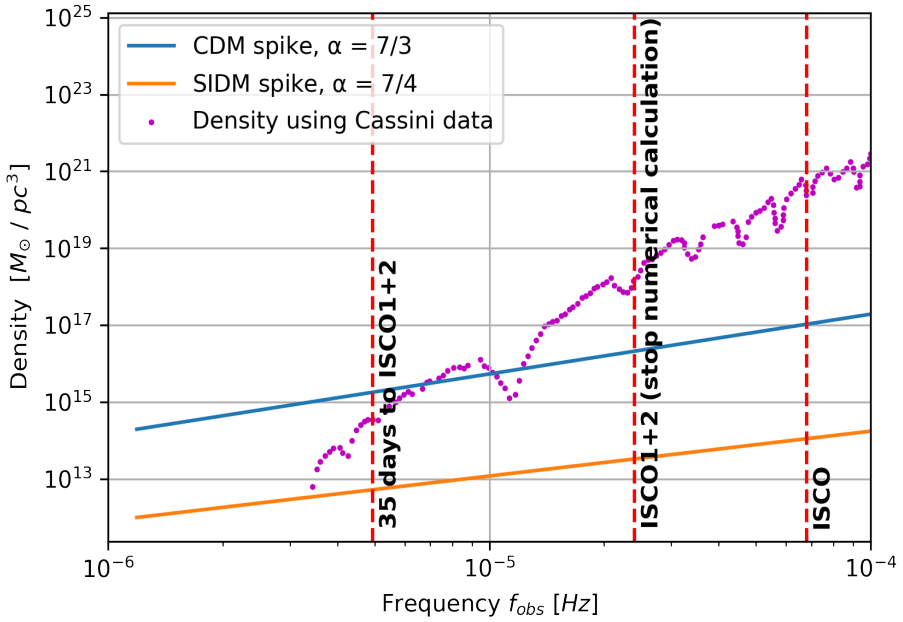

Fig. 4.14: The lower limit for the DM density by using the Cassini data is depicted in violet. For comparison, the DM density distribution for the corresponding CDM (blue) and SIDM (orange) spike is also plotted. Additionally, three different frequencies are marked, and their labels indicate the respective separation r between the SMBHs. The label "35 days to ISCO1+2" corresponds to the initial frequency f_{ini}. When the SMBHs reach the separation of $r = r_{ISCO,1} + r_{ISCO,2}$, the numerical calculation is terminated. Furthermore, the ISCO of one of the SMBHs is marked as a reference value. Again, static, non-relativistic spikes and circular orbits are assumed. $\{D,\, m,\, \sigma,\, b_{max}\,,\, \iota\} = \{65\,\mathrm{Mpc},\, 9 \times 10^7\, M_\odot,\, 200\,\mathrm{km/s},\, 10\,\mathrm{kpc},\, \pi/2\}$.

In the above plot, it is evident that both the density distribution of the CDM spike and that of the SIDM spike mostly lie below the lower limit of the DM density around SMBHs in the relevant frequency range. Unfortunately, this problem occurs for all possible combinations of D and m for which this lower bound behaves in a physically meaningful way (i.e., takes only positive values). Using (rotating) SIDM spikes to constrain the mass interval from Chapter 4.2 would ultimately only lead to finding a different combination of D and m that minimizes the total absolute deviation Δ. In the case of rotating CDM spikes, f_{ini} is about an order of magnitude smaller than for static CDM spikes (cf. Table 4.2). The corresponding SNR should approach zero according to Figure 4.11.

Since the lower limit is not completely below the density distribution for CDM spikes for all detectable D and m, neither of the two models can be ruled out. In summary, it can be noted that the data from Cassini is less suitable for assuming an individual nearby SMBHB dominating a part of the GWB. If this assumption is nevertheless made, Figure 4.14 shows that the case involving CDM spikes around SMBHs is more likely than the one involving SIDM spikes.

To constrain the particle properties of DM, one requires a GW signal from an individual SMBHB with known parameters such as mass and luminosity distance. The attempt to determine the values of these parameters by minimizing Δ, i.e., choosing the most suitable combination for D and m such that the characteristic strain h_c of the GW signal from this selected SMBHB best matches $h_{c,Cassini}$ within the relevant frequency range, has proven to be not very successful.

If it becomes possible in the future to detect GWs from individual SMBHBs, and if these binaries satisfy the conditions mentioned in Chapter 2.5, one can calculate the density of DM in their vicinity using Equation (2.71). By comparing the results with the density distributions in the case of CDM and SIDM spikes, potential constraints on the matter environment of SMBHs could be derived.

5 Conclusions

In this work it has been illustrated that the presence of DM spikes around the SMBHs of a SMBHB can leave clearly visible fingerprints in the GW signal emitted by this system. The depth of these fingerprints depends on the particle properties of DM. It has been shown that in the final phase of the SMBHB evolution, the characteristic strain in the case with CDM spikes can be better distinguished from that of the vacuum case because of the higher density in the central region of the spikes, in contrast to the situation with SIDM spikes. In this context, it was important to consider the dynamical friction due to the gravitational interaction of the SMBHs with DM particles. Therefore, a formula describing this effect for different system properties, such as static or rotating spikes, was derived. One drawback of the model is that it does not take into account interactions between DM particles. The resulting energy transfer within the spikes could have a significant impact on the evolution of SMBHBs. This can be explored in future works.

The main focus of this bachelor thesis was to use the upper bound on the GWB from the Cassini spacecraft to determine a lower limit for the DM density around SMBHs. By directly comparing this lower limit with the density distributions of CDM and SIDM spikes, the aim was to find out which of these two DM theories could be considered more appropriate for describing DM spikes around SMBHs. Unfortunately, the assumptions made are not well-suited to make clear statements or to draw definitive conclusions, since the density distributions for CDM and SIDM spikes are mainly below the lower limit. Nevertheless, at the current stage, it would not have been possible to use the Cassini data within this research without these assumptions, since it is not yet possible to filter out GW signals from the GWB and attribute them to individual sources.

However, I am not aware of any previous research in this field that specifically addresses this particular and, in my opinion, promising method for constraining the properties of DM particles in this frequency range. All that is missing are GW signals that can be unambiguously attributed to individual SMBHBs in the final phase of their evolution. The Laser Interferometer Space Antenna (LISA) should have the potential to measure these GWs in the future [52].

6 Outlook

Another way to gain information about the matter environment of SMBHs is to study the stochastic GWB in the *nanohertz* range. As mentioned at the beginning of this work, the GW signals from SMBHBs are located in this frequency range during the early phase of their evolution. Interestingly, the shape of the characteristic strain of this astrophysical background could provide insights into the properties of the matter surrounding the SMBHs, as discussed in [36] or [46]. The measurement data on this GWB from Pulsar Timing Arrays[18] (PTAs) seems to be promising for this purpose, especially in the light of the recent publications of the 15-year data set (see [53]–[55]) by NANOGrav[19].

Acknowledgements

At this point, I would like to express my gratitude to Prof. Dr. Laura Sagunski for her support and for giving me the opportunity to work on this very interesting and fascinating topic. I also thank Prof. Kris Pardo and Alexander Huhn for the insightful discussions during this project. I look forward to our future collaboration.
Furthermore, I would like to thank Prof. Dr. Jürgen Schaffner-Bielich for his work as second reviewer of this bachelor thesis.
Last but not least, I extend my appreciation to all the proofreaders of this work, including some of my closest friends and family members.

[18] PTAs: Here, the variations in time of the arrival of periodic signals emitted by a set of millisecond pulsars are used to measure the stochastic GWB. These temporal changes are caused by GWs passing between the Earth and the pulsars.
[19] NANOGrav: An international collaboration to study low-frequency GWs by PTAs.

References

[1] D. Castelvecchi and A. Witze, "Einstein's gravitational waves found at last," *Nature News*, 2016. DOI: 10.1038/nature.2016.19361.

[2] M. Maggiore, *Gravitational Waves. Vol. 2: Astrophysics and Cosmology*. Oxford University Press, 2018. DOI: 10.1093/oso/9780198570899.001.0001.

[3] B. P. Abbott, *et al.*, "Observation of gravitational waves from a binary black hole merger," *Physical Review Letters*, 2016. DOI: 10.1103/physrevlett.116.061102.

[4] B. P. Abbott, *et al.*, "Improved analysis of GW150914 using a fully spin-precessing waveform model," *Physical Review X*, 2016. DOI: 10.1103/physrevx.6.041014.

[5] P. Athron, C. Balázs, A. Fowlie, L. Morris, and L. Wu, *Cosmological phase transitions: From perturbative particle physics to gravitational waves*, 2023. arXiv: 2305.02357 [hep-ph].

[6] C. J. Moore, R. H. Cole, and C. P. L. Berry, "Gravitational-wave sensitivity curves," *Classical and Quantum Gravity*, 2014. DOI: 10.1088/0264-9381/32/1/015014.

[7] K. Boshkayev, T. Konysbayev, Y. Kurmanov, *et al.*, *Numerical analyses of m31 dark matter profiles*, 2022. arXiv: 2212.02999 [gr-qc].

[8] S. Das and S. Sur, *Gravitational lensing and missing mass*, 2023. arXiv: 2303.03259 [gr-qc].

[9] G. Bertone, *Particle Dark Matter: Observations, Models and Searches*. Cambridge University Press, 2010. DOI: 10.1017/CBO9780511770739.

[10] G. Mohan and U. D. Goswami, *Galactic rotation curves of spiral galaxies and dark matter in $f(\mathcal{R}, T)$ gravity theory*, 2022. arXiv: 2211.02948 [gr-qc].

[11] G. Pascoli, *An empirical analysis of the dynamics of both individual galaxies and gravitational lensing in galaxy clusters without dark matter*, 2022. arXiv: 2210.12380 [astro-ph.GA].

[12] S. Hossenfelder and S. S. McGaugh, "Is dark matter real?" *Scientific American*, 2018. DOI: 10.1038/scientificamerican0818-36.

[13] D. Clowe, M. Bradač, A. H. Gonzalez, *et al.*, "A direct empirical proof of the existence of dark matter," *The Astrophysical Journal*, 2006. DOI: 10.1086/508162.

[14] J. W. Armstrong, L. Iess, P. Tortora, and B. Bertotti, "Stochastic gravitational wave background: Upper limits in the 10-6 to 10-3 hz band," *The Astrophysical Journal*, 2003. DOI: 10.1086/379505.

[15] B. Bertotti, A. Vecchio, and L. Iess, "Gravitational waves from coalescing binaries and doppler experiments," *Physical Review D*, 1999. DOI: 10.1103/physrevd.59.082001.

[16] S. Abbate, J. Armstrong, S. Asmar, *et al.*, "The cassini gravitational wave experiment," 2003. DOI: 10.1117/12.458566.

[17] G. Bertone and T. M. P. Tait, "A new era in the search for dark matter," *Nature*, 2018. DOI: 10.1038/s41586-018-0542-z.

[18] J. Mimouni, "Xxist century perspectives on the micro macro worlds," *Journal of Physics: Conference Series*, 2021. DOI: 10.1088/1742-6596/1766/1/012001.

[19] G. Gentile, P. Salucci, U. Klein, D. Vergani, and P. Kalberla, "The cored distribution of dark matter in spiral galaxies," *Monthly Notices of the Royal Astronomical Society*, 2004. DOI: 10.1111/j.1365-2966.2004.07836.x.

[20] J. F. Navarro, C. S. Frenk, and S. D. M. White, "The structure of cold dark matter halos," *The Astrophysical Journal*, 1996. DOI: 10.1086/177173.

[21] S. Tulin and H.-B. Yu, "Dark matter self-interactions and small scale structure," *Physics Reports*, 2018. DOI: 10.1016/j.physrep.2017.11.004.

[22] Q. L. Nguyen, G. J. Mathews, L. A. Phillips, M. A. Correa, I.-S. Suh, and J. W. Coughlin, "3-3-1 self interacting dark matter and the galaxy core-cusp problem," *Modern Physics Letters A*, 2020. DOI: 10.1142/s0217732321300019.

[23] D. N. Spergel and P. J. Steinhardt, "Observational evidence for self-interacting cold dark matter," *Physical Review Letters*, 2000. DOI: 10.1103/physrevlett.84.3760.

[24] K. Desai, R. Li, and S. Meighen-Berger, *Searching for dark matter annihilation with icecube and p-one*, 2023. arXiv: 2302.10542 [hep-ph].

[25] H. C. Turner, M. R. Lovell, J. Zavala, and M. Vogelsberger, "The onset of gravothermal core collapse in velocity-dependent self-interacting dark matter subhaloes," *Monthly Notices of the Royal Astronomical Society*, 2021. DOI: 10.1093/mnras/stab1725.

[26] F.-Y. Cyr-Racine, K. Sigurdson, J. Zavala, T. Bringmann, M. Vogelsberger, and C. Pfrommer, "ETHOS - an effective theory of structure formation: From dark particle physics to the matter distribution of the universe," *Physical Review D*, 2016. DOI: 10.1103/physrevd.93.123527.

[27] O. D. Elbert, J. S. Bullock, S. Garrison-Kimmel, M. Rocha, J. Oñ orbe, and A. H. G. Peter, "Core formation in dwarf haloes with self-interacting dark matter: No fine-tuning necessary," *Monthly Notices of the Royal Astronomical Society*, 2015. DOI: 10.1093/mnras/stv1470.

[28] P. Gondolo and J. Silk, "Dark matter annihilation at the galactic center," *Physical Review Letters*, 1999. DOI: 10.1103/physrevlett.83.1719.

[29] T. Lacroix, "Dynamical constraints on a dark matter spike at the galactic centre from stellar orbits," *Astronomy &amp Astrophysics*, 2018. DOI: 10.1051/0004-6361/201832652.

[30] F. M. Khan, "Dynamics and evolution of supermassive black holes in merging galaxies," *Astronomisches Rechen-Institut, Zentrum für Astronomie der Universität Heidelberg*, 2011. [Online]. Available: https://www.imprs-hd.mpg.de/56059/thesis_khan.pdf.

[31] K. Eda, Y. Itoh, S. Kuroyanagi, and J. Silk, "Gravitational waves as a probe of dark matter minispikes," *Physical Review D*, 2015. DOI: 10.1103/physrevd.91.044045.

[32] S. L. Shapiro and V. Paschalidis, "Self-interacting dark matter cusps around massive black holes," *Physical Review D*, 2014. DOI: 10.1103/physrevd.89.023506.

[33] N. Aghanim, Y. Akrami, M. Ashdown, *et al.*, "Planck 2018 results. i. overview and the cosmological legacy of planck," *Astronomy &amp Astrophysics*, 2020. DOI: 10.1051/0004-6361/201833910.

[34] M. Colpi, P. Casella, V. Gorini, U. Moschella, and A. Possenti, *Physics of Relativistic Objects in Compact Binaries: From Birth to Coalescence*. 2009. DOI: 10.1007/978-1-4020-9264-0.

[35] M. Celoria, R. Oliveri, A. Sesana, and M. Mapelli, *Lecture notes on black hole binary astrophysics*, 2018. arXiv: 1807.11489 [astro-ph.GA].

[36] Z.-Q. Shen, G.-W. Yuan, Y.-Y. Wang, and Y.-Z. Wang, *Dark matter spike surrounding supermassive black holes binary and the nanohertz stochastic gravitational wave background*, 2023. arXiv: 2306.17143 [astro-ph.HE].

[37] J. Binney and S. Tremaine, *Galactic Dynamics: Second Edition*. Princeton University Press, 2008. DOI: 10.1515/9781400828722.

[38] S. Noble, J. Kazmierczak, S. Noble, and S. Wiessinger, *Supermassive black hole binary simulation visualizations in 4k*, 2023. [Online]. Available: https://svs.gsfc.nasa.gov/13086.

[39] B. J. Kavanagh, D. A. Nichols, G. Bertone, and D. Gaggero, "Detecting dark matter around black holes with gravitational waves: Effects of dark-matter dynamics on the gravitational waveform," *Physical Review D*, 2020. DOI: 10.1103/physrevd.102.083006.

[40] J. Yu, *The influence of self interacting dark matter on dynamical friction time scale and the final parsec problem*, 2021. [Online]. Available: https://mercersec.org/fair/projects/project/389.

[41] E. Barausse, "Relativistic dynamical friction in a collisional fluid," *Monthly Notices of the Royal Astronomical Society*, 2007. DOI: 10.1111/j.1365-2966.2007.12408.x.

[42] N. Speeney, A. Antonelli, V. Baibhav, and E. Berti, "Impact of relativistic corrections on the detectability of dark-matter spikes with gravitational waves," *Physical Review D*, 2022. DOI: 10.1103/physrevd.106.044027.

[43] M. C. Begelman, R. D. Blandford, and M. J. Rees, "Massive black hole binaries in active galactic nuclei," 1980. DOI: 10.1038/287307a0.

[44] M. Maggiore, *Gravitational Waves. Vol. 1: Theory and Experiments*. Oxford University Press, 2007. DOI: 10.1093/acprof:oso/9780198570745.001.0001.

[45] N. Becker, L. Sagunski, L. Prinz, and S. Rastgoo, "Circularization versus eccentrification in intermediate mass ratio inspirals inside dark matter spikes," *Physical Review D*, 2022. DOI: 10.1103/physrevd.105.063029.

[46] G. Sato-Polito and M. Kamionkowski, *Exploring the spectrum of stochastic gravitational-wave anisotropies with pulsar timing arrays*, 2023. arXiv: 2305.05690 [astro-ph.CO].

[47] A. Coogan, G. Bertone, D. Gaggero, B. J. Kavanagh, and D. A. Nichols, "Measuring the dark matter environments of black hole binaries with gravitational waves," *Physical Review D*, 2022. DOI: 10.1103/physrevd.105.043009.

[48] N. Aggarwal, O. D. Aguiar, A. Bauswein, *et al.*, "Challenges and opportunities of gravitational-wave searches at MHz to GHz frequencies," *Living Reviews in Relativity*, 2021. DOI: 10.1007/s41114-021-00032-5.

[49] D. A. Forbes and T. J. Ponman, "On the relationship between age and dynamics in elliptical galaxies," *Monthly Notices of the Royal Astronomical Society*, 1999. DOI: 10.1046/j.1365-8711.1999.02868.x.

[50] M. Enoki, K. T. Inoue, M. Nagashima, and N. Sugiyama, "Gravitational waves from supermassive black hole coalescence in a hierarchical galaxy formation model," *The Astrophysical Journal*, 2004. DOI: 10.1086/424475.

[51] A. Vecchio, B. Bertotti, and L. Iess, *Coalescing binaries and doppler experiments*, 1997. arXiv: gr-qc/9708033 [gr-qc].

[52] P. Amaro-Seoane, J. Andrews, M. A. Sedda, *et al.*, "Astrophysics with the laser interferometer space antenna," *Living Reviews in Relativity*, 2023. DOI: 10.1007/s41114-022-00041-y.

[53] G. Agazie, A. Anumarlapudi, A. M. Archibald, *et al.*, "The nanograv 15-year data set: Evidence for a gravitational-wave background," *The Astrophysical Journal Letters*, 2023. DOI: 10.3847/2041-8213/acdac6.

[54] G. Agazie, A. Anumarlapudi, A. M. Archibald, *et al.*, *The nanograv 15-year data set: Constraints on supermassive black hole binaries from the gravitational wave background*, 2023. arXiv: 2306.16220 [astro-ph.HE].

[55] G. Agazie, A. Anumarlapudi, A. M. Archibald, *et al.*, *The nanograv 15-year data set: Bayesian limits on gravitational waves from individual supermassive black hole binaries*, 2023. arXiv: 2306.16222 [astro-ph.HE].